

# Hierarchical Multiscale Mechanism Development for Methane Partial Oxidation and Reforming and for Thermal Decomposition of Oxygenates on Rh

A. B. Mhadeshwar and D. G. Vlachos\*

Department of Chemical Engineering and Center for Catalytic Science and Technology,  
University of Delaware, Newark, Delaware 19716-3110

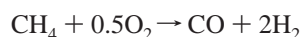
Received: May 11, 2005; In Final Form: July 9, 2005

A thermodynamically consistent  $C_1$  microkinetic model is developed for methane partial oxidation and reforming and for oxygenate (methanol and formaldehyde) decomposition on Rh via a hierarchical multiscale methodology. Sensitivity analysis is employed to identify the important parameters of the semiempirical unity bond index quadratic exponential potential (UBI-QEP) method and these parameters are refined using quantum mechanical density functional theory. With adjustment of *only two* pre-exponentials in the  $CH_4$  oxidation subset, the  $C_1$  mechanism captures a multitude of catalytic partial oxidation (CPOX) and reforming experimental data as well as thermal decomposition of methanol and formaldehyde. We validate the microkinetic model against high-pressure, spatially resolved CPOX experimental data. Distinct oxidation and reforming zones are predicted to exist, in agreement with experiments, suggesting that hydrogen is produced from reforming of methane by  $H_2O$  formed in the oxidation zone. CO is produced catalytically by partial oxidation up to moderately high pressures, with water-gas shift taking place in the gas-phase at sufficiently high pressures resulting in reduction of CO selectivity.

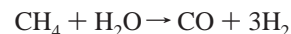
## Introduction

Hydrogen is considered as the fuel of the 21st century due to its potential applications in power generation. Eight major automobile companies have announced plans to commercialize fuel cell vehicles in this decade.<sup>1</sup> Portable fuel cell generators for industrial applications are already available in the market.<sup>2</sup> The idea of a hydrogen economy, however, will thrive upon clean and economic conversion of fuels, such as natural gas, coal, biomass, etc., to syngas. Syngas is also used in many other processes including methanol, ammonia, and gasoline production. Steam reforming of methane is currently the preferred path for hydrogen production from natural gas. Autothermal and dry reforming of natural gas are also of potential interest. Catalytic partial oxidation (CPOX) of methane in short contact time reactors<sup>3</sup> is yet another route, in which, rhodium (Rh) was found to be a very efficient catalyst giving high methane conversion and syngas selectivity. Methanol decomposition is another important reaction for hydrogen production due to its application in direct methanol fuel cells (DMFC). Water–gas shift (WGS) is typically used to convert the unwanted carbon monoxide into hydrogen, followed by preferential oxidation of CO (PROX) to reduce CO to levels acceptable for proton exchange membrane (PEM) fuel cells. The overall reactions for  $H_2$  production can be given as (the autothermal reforming stoichiometry is chosen for illustration to be the sum of CPOX and steam reforming ones)

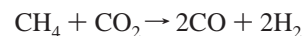
Partial oxidation:



Steam reforming:



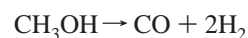
Dry reforming:



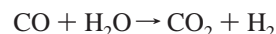
Autothermal reforming:



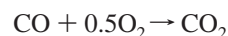
Methanol decomposition:



Water–gas shift:



CO combustion:



$H_2$  combustion:



In recent work, we have demonstrated that there is a need for developing reliable, predictive microkinetic models for complex fuel processing applications describing the above reactions, since currently available literature models suffer from a number of shortcomings outlined in refs 4–7. Most literature models are thermodynamically inconsistent, an inherent requirement for correct prediction of equilibrium.<sup>8</sup> Furthermore, they do not include the effect of adsorbate–adsorbate interactions on activation energies of surface kinetics; they lack important reaction paths and are typically tuned to capture a single type of experimental data over a narrow range of operating conditions. We provide specific examples of such limitations later.

\* Corresponding author. Phone: (302) 831-2830. Fax: (302) 831-1048.  
E-mail: vlachos@che.Udel.edu.

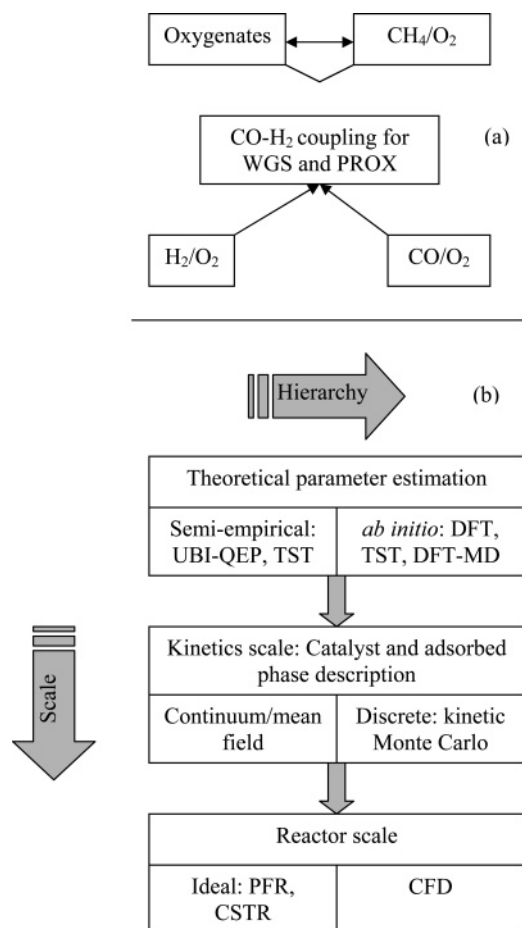


**Figure 1.** Panel a shows the schematic representation of the bottom-up development of the  $C_1$  surface reaction mechanism on Rh, whereas panel b shows the generalized hierarchical multiscale modeling approach.

To overcome these limitations, we have developed a hierarchical multiscale approach for the development of predictive surface reaction mechanisms (see refs 9–11 for some elements of this approach). As shown in Figure 1a, this is a bottom-up approach, in which elementary-like reaction mechanisms are first developed for simpler fuels, followed by addition of reactions for more complex fuels or reaction sets that account for coupling or synergism arising from having multiple fuels. As an example, before developing a mechanism for methane oxidation and reforming on Rh, we first developed thermodynamically consistent mechanisms for CO oxidation,  $H_2$  oxidation, followed by a CO– $H_2$  coupling mechanism that captures WGS and PROX on Rh.<sup>11</sup> Coupling happens for example in PROX, where both CO and  $H_2$  are cofed to a reactor, but also in CPOX where all of the above reactions can occur simultaneously or in different spatial regions of a reactor. Since reforming and WGS reactions can be equilibrium limited at the high temperatures of CPOX, having a thermodynamically consistent reaction model is important in order to assess their role in CPOX.

In this paper, we extend the application of this hierarchical multiscale approach to develop a new thermodynamically consistent microkinetic  $C_1$  model on Rh for methane CPOX and reforming as well as thermal decomposition of  $C_1$  oxygenates (methanol and formaldehyde). The paper is organized as follows. First we discuss the development of a thermodynamically consistent  $C_1$  mechanism on Rh. Hierarchical refinement of the important parameters is carried out. Validation of the  $C_1$

mechanism is presented against high-pressure, spatially resolved CPOX experimental data. Then we present an analysis of the  $C_1$  mechanism at various pressures to elucidate the important reaction paths (e.g., direct versus indirect CPOX mechanism) and the effect of gas-phase chemistry. Finally, the  $C_1$  mechanism is validated against  $CH_4$  reforming and oxygenate thermal decomposition experiments, followed by conclusions. Additional validation of the  $C_1$  mechanism against atmospheric pressure CPOX experiments is shown in the Appendix.

### A Thermodynamically Consistent $C_1$ Mechanism on Rh

The overall approach of making a mechanism thermodynamically consistent was introduced in ref 8. Here we give some specifics for the  $C_1$  mechanism. The CO– $H_2$  coupling mechanism consists of 46 reactions ( $R_1$ – $R_{46}$ ), as shown in Table 1, and is taken from ref 11. This mechanism consists of the CO and  $H_2$  oxidation subsets whose parameters were simultaneously optimized and validated against multiple experimental data. It also consists of a CO– $H_2$  coupling subset, which captures WGS and PROX data with the adjustment of two kinetic rate parameters and of the catalyst area per reactor volume,  $A/V$ . None of these parameters has been adjusted in this work despite some of them being very important for the processes discussed here.

Here, a set of 58 elementary-like reactions is added ( $R_{47}$ – $R_{104}$ ) for  $CH_4$  oxidation and oxygenate thermal decomposition. These reactions mainly include dissociative adsorption of  $CH_4$ , adsorption and desorption of  $CH_x$  species, thermal dehydrogenation of  $CH_x$  species, oxidative dehydrogenation of  $CH_x$  species by  $O^*$  and  $OH^*$ , thermal decomposition of CO, the reverse Boudouard reaction, and oxygenate decomposition reactions. Oxygenate decomposition steps are important to connect methane as well as syngas to methanol and formaldehyde decomposition for hydrogen production for fuel cells. Reaction steps ( $R_{47}$ – $R_{82}$ ) involving  $CH_4$  are taken from previous work on Pt.<sup>12</sup> The oxygenate decomposition steps ( $R_{83}$ – $R_{104}$ ) are taken from the Pt work of refs 13 and 14.

The reaction rate constant ( $k$ ) is calculated using the modified Arrhenius form

$$k = \frac{A}{\sigma^{n-1}} \left( \frac{T}{T_0} \right)^\beta e^{-E/(R_g T)}$$

or

$$k = \frac{s}{\sigma^n} \sqrt{\frac{R_g T}{2\pi M}} \left( \frac{T}{T_0} \right)^\beta e^{-E/(R_g T)}$$

Here  $A$  is the pre-exponential,  $s$  is the sticking coefficient,  $\sigma$  is the site density,  $n$  is the reaction order,  $\beta$  is the temperature exponent,  $E$  is the activation energy,  $R_g$  is the ideal gas constant, and  $T$  is the absolute temperature. For the additional 58 reactions, nominal values of the pre-exponentials are initially set using transition state theory (TST), e.g.,  $10^{13} \text{ s}^{-1}$  for desorption and  $10^{11} \text{ s}^{-1}$  for Langmuir–Hinshelwood type surface reactions, based on ref 15. Sticking coefficients of  $CH_x$  and oxygenate species are initially assumed as unity. The molecular heat of chemisorption ( $Q$ ) of  $CH_4$  is taken as 6 kcal/mol based on the chemisorption experiments of ref 16.  $Q_C$  and  $Q_{CH_3}$  are available from the density functional theory (DFT) results of refs 17 and 18, respectively. However,  $Q_{CH}$  and  $Q_{CH_2}$  have not been reported in the literature. Therefore, they are calculated using the semiempirical unity bond index quadratic exponential potential (UBI-QEP) method (also known as bond

**TABLE 1: Surface Reaction Mechanisms for CO Oxidation (R<sub>1</sub>–R<sub>10</sub>), H<sub>2</sub> Oxidation (R<sub>1</sub>–R<sub>4</sub> and R<sub>11</sub>–R<sub>24</sub>), CO–H<sub>2</sub> Coupling (R<sub>1</sub>–R<sub>46</sub>), and C<sub>1</sub> (R<sub>47</sub>–R<sub>104</sub> Mainly for CH<sub>4</sub> and R<sub>83</sub>–R<sub>104</sub> Mainly for Oxygenate Decomposition) Reactions on Rh<sup>a</sup>**

no.	reaction	sticking coefficient (unitless) or pre-exponential (s <sup>-1</sup> )	temperature exponent $\beta$	activation energy (kcal/mol) and {typical estimates in oxidation zone and reforming zone of CPOX at 1373 K}
Oxygen Adsorption–Desorption Steps				
R <sub>1</sub>	O <sub>2</sub> + 2* → 2O*	4.81 × 10 <sup>-2</sup>	1.997	0.0 {0.0, 0.0}
R <sub>2</sub>	2O* → O <sub>2</sub> + 2*	4.31 × 10 <sup>12</sup>	1.199	80.9 – 42θ <sub>O</sub> + $f(T)$ {42.9, 72.3}
R <sub>3</sub>	O + * → O*	4.45 × 10 <sup>-2</sup>	-1.895	0.0 {0.0, 0.0}
R <sub>4</sub>	O* → O + *	9.76 × 10 <sup>12</sup>	-1.999	100 – 21θ <sub>O</sub> + $f(T)$ {11.0, 10.6}
CO Oxidation on Rh				
R <sub>5</sub>	CO + * → CO*	5.00 × 10 <sup>-1</sup>	-2.000	0.0 {0.0, 0.0}
R <sub>6</sub>	CO* → CO + *	2.26 × 10 <sup>14</sup>	1.988	38.5 – 17θ <sub>CO</sub> – 3.7θ <sub>H</sub> + $f(T)$ {34.2, 33.9}
R <sub>7</sub>	CO <sub>2</sub> + * → CO <sub>2</sub> *	9.77 × 10 <sup>-2</sup>	-1.946	0.0 {0.0, 0.0}
R <sub>8</sub>	CO <sub>2</sub> * → CO <sub>2</sub> + *	1.13 × 10 <sup>13</sup>	1.800	5.2 + $f(T)$ {0.9, 0.9}
R <sub>9</sub>	CO <sub>2</sub> * + * → CO* + O*	2.04 × 10 <sup>10</sup>	1.545	17.3 + $f(\theta_O, \theta_H, \theta_{CO}, T)$ {29.3, 18.5} <sup>b</sup>
R <sub>10</sub>	CO* + O* → CO <sub>2</sub> * + *	1.17 × 10 <sup>9</sup>	1.781	23.5 + $f(\theta_O, \theta_H, \theta_{CO}, T)$ {16.8, 20.5} <sup>c</sup>
H <sub>2</sub> Oxidation on Rh				
R <sub>11</sub>	H <sub>2</sub> + 2* → 2H*	7.73 × 10 <sup>-1</sup>	0.939	0.0 {0.0, 0.0}
R <sub>12</sub>	2H* → H <sub>2</sub> + 2*	5.56 × 10 <sup>11</sup>	-0.435	20.4 – 5θ <sub>H</sub> – 7.4θ <sub>CO</sub> + $f(T)$ {11.0, 10.6}
R <sub>13</sub>	OH* + * → H* + O*	1.41 × 10 <sup>11</sup>	-0.375	24.2 + $f(\theta_O, \theta_H, \theta_{H_2O}, \theta_{CO}, T)$ {20.5, 25.9}
R <sub>14</sub>	H* + O* → OH* + *	1.73 × 10 <sup>10</sup>	-0.710	14.2 + $f(\theta_O, \theta_H, \theta_{H_2O}, \theta_{CO}, T)$ {13.9, 10.7}
R <sub>15</sub>	H <sub>2</sub> O* + * → H* + OH*	3.79 × 10 <sup>11</sup>	0.828	15.4 + $f(\theta_O, \theta_H, \theta_{OH}, \theta_{H_2O}, \theta_{CO}, T)$ {26.1, 17.1}
R <sub>16</sub>	H* + OH* → H <sub>2</sub> O* + *	4.73 × 10 <sup>10</sup>	0.498	17.6 + $f(\theta_O, \theta_H, \theta_{OH}, \theta_{H_2O}, \theta_{CO}, T)$ {0.0, 13.9}
R <sub>17</sub>	H <sub>2</sub> O* + O* → 2OH*	1.87 × 10 <sup>10</sup>	-0.918	11.4 + $f(\theta_O, \theta_{OH}, \theta_{H_2O}, T)$ {20.4, 10.4}
R <sub>18</sub>	2OH* → H <sub>2</sub> O* + O*	3.20 × 10 <sup>10</sup>	-1.485	23.6 + $f(\theta_O, \theta_{OH}, \theta_{H_2O}, T)$ {0.9, 22.5}
R <sub>19</sub>	OH + * → OH*	5.59 × 10 <sup>-2</sup>	0.354	0.0 {0.0, 0.0}
R <sub>20</sub>	OH* → OH + *	5.42 × 10 <sup>13</sup>	-1.593	70 – 33θ <sub>O</sub> + 25θ <sub>H<sub>2</sub>O</sub> + $f(T)$ {42.6, 65.7}
R <sub>21</sub>	H <sub>2</sub> O + * → H <sub>2</sub> O*	7.72 × 10 <sup>-2</sup>	1.407	0.0 {0.0, 0.0}
R <sub>22</sub>	H <sub>2</sub> O* → H <sub>2</sub> O + *	2.06 × 10 <sup>13</sup>	-1.861	10.8 – 4.5θ <sub>H<sub>2</sub>O</sub> + 25θ <sub>OH</sub> + $f(T)$ {5.5, 5.5}
R <sub>23</sub>	H + * → H*	1.63 × 10 <sup>-1</sup>	1.688	0.0 {0.0, 0.0}
R <sub>24</sub>	H* → H + *	2.83 × 10 <sup>12</sup>	1.164	62.3 – 2.5θ <sub>H</sub> – 3.7θ <sub>CO</sub> + $f(T)$ {59.1, 58.3}
Coupling between CO and H <sub>2</sub> Chemistries on Rh				
R <sub>25</sub>	CO <sub>2</sub> * + H* → CO* + OH*	1.07 × 10 <sup>11</sup>	0.030	4.4 + $f(\theta_O, \theta_H, \theta_{H_2O}, \theta_{CO}, T)$ {12.4, 2.6}
R <sub>26</sub>	CO* + OH*** → CO <sub>2</sub> * + H*	9.38 × 10 <sup>10</sup>	-0.030	20.5 + $f(\theta_O, \theta_H, \theta_{H_2O}, \theta_{CO}, T)$ {6.6, 19.8}
R <sub>27</sub>	COOH + * → COOH*	1.51 × 10 <sup>-2</sup>	-0.938	0.0 {0.0, 0.0}
R <sub>28</sub>	COOH* → COOH + *	4.69 × 10 <sup>13</sup>	0.938	62.2 + $f(T)$ {56.9, 56.9}
R <sub>29</sub>	COOH* + * → CO* + OH*	4.83 × 10 <sup>11</sup>	-0.397	6.2 + $f(\theta_O, \theta_H, \theta_{H_2O}, \theta_{CO}, T)$ {16.4, 6.7}
R <sub>30</sub>	CO* + OH* → COOH* + *	2.07 × 10 <sup>10</sup>	0.397	18.6 + $f(\theta_O, \theta_H, \theta_{H_2O}, \theta_{CO}, T)$ {2.6, 15.7}
R <sub>31</sub>	COOH* + * → CO <sub>2</sub> * + H*	4.57 × 10 <sup>10</sup>	-0.434	4.2 + $f(\theta_H, \theta_{CO}, T)$ {7.9, 8.1}
R <sub>32</sub>	CO <sub>2</sub> * + H* → COOH* + *	2.19 × 10 <sup>9</sup>	0.434	0.6 + $f(\theta_H, \theta_{CO}, T)$ {0.0, 0.0}
R <sub>33</sub>	CO* + H <sub>2</sub> O* → COOH* + H*	7.15 × 10 <sup>10</sup>	0.440	20.7 + $f(\theta_H, \theta_{OH}, \theta_{H_2O}, \theta_{CO}, T)$ {20.7, 20.6}
R <sub>34</sub>	COOH* + H* → CO* + H <sub>2</sub> O*	1.40 × 10 <sup>11</sup>	-0.440	10.5 + $f(\theta_H, \theta_{OH}, \theta_{H_2O}, \theta_{CO}, T)$ {8.3, 8.3}
R <sub>35</sub>	CO <sub>2</sub> * + OH* → COOH* + O*	9.54 × 10 <sup>10</sup>	0.200	22.3 + $f(\theta_O, \theta_{H_2O}, T)$ {16.1, 21.5}
R <sub>36</sub>	COOH* + O* → CO <sub>2</sub> * + OH*	1.05 × 10 <sup>11</sup>	-0.200	16.0 + $f(\theta_O, \theta_{H_2O}, T)$ {17.5, 14.4}
R <sub>37</sub>	CO <sub>2</sub> * + H <sub>2</sub> O* → COOH* + OH*	7.44 × 10 <sup>10</sup>	0.479	13.5 + $f(\theta_O, \theta_{OH}, \theta_{H_2O}, T)$ {21.3, 12.8}
R <sub>38</sub>	COOH* + OH* → CO <sub>2</sub> * + H <sub>2</sub> O*	1.34 × 10 <sup>11</sup>	-0.479	19.4 + $f(\theta_O, \theta_{OH}, \theta_{H_2O}, T)$ {3.1, 17.7}
R <sub>39</sub>	HCOO + 2* → HCOO**	1.89 × 10 <sup>-2</sup>	-0.555	0.0 {0.0, 0.0}
R <sub>40</sub>	HCOO** → HCOO + 2*	3.74 × 10 <sup>13</sup>	0.555	69.2 + $f(T)$ {62.8, 62.8}
R <sub>41</sub>	CO <sub>2</sub> * + H* → HCOO**	1.40 × 10 <sup>10</sup>	0.654	4.2 + $f(\theta_H, \theta_{CO}, T)$ {0.5, 0.3}
R <sub>42</sub>	HCOO** → CO <sub>2</sub> * + H*	7.12 × 10 <sup>11</sup>	-0.654	0.0 + $f(\theta_H, \theta_{CO}, T)$ {0.0, 0.0}
R <sub>43</sub>	CO <sub>2</sub> * + OH* + * → HCOO** + O*	5.97 × 10 <sup>10</sup>	0.431	27.5 + $f(\theta_O, \theta_{H_2O}, T)$ {21.3, 26.8}
R <sub>44</sub>	HCOO** + O* → CO <sub>2</sub> * + OH* + *	1.67 × 10 <sup>11</sup>	-0.431	13.4 + $f(\theta_O, \theta_{H_2O}, T)$ {14.2, 11.3}
R <sub>45</sub>	CO <sub>2</sub> * + H <sub>2</sub> O* + * → HCOO** + OH*	4.78 × 10 <sup>10</sup>	0.696	18.4 + $f(\theta_O, \theta_{OH}, \theta_{H_2O}, T)$ {26.6, 17.8}
R <sub>46</sub>	HCOO** + OH* → CO <sub>2</sub> * + H <sub>2</sub> O* + *	2.09 × 10 <sup>11</sup>	-0.696	16.4 + $f(\theta_O, \theta_{OH}, \theta_{H_2O}, T)$ {0.0, 14.3}
CH <sub>4</sub> Oxidation and Reforming on Rh				
R <sub>47</sub>	C + * → C*	5.61 × 10 <sup>-2</sup>	-1.704	0.0 {0.0, 0.0}
R <sub>48</sub>	C* → C + *	1.26 × 10 <sup>13</sup>	1.704	159 + $f(T)$ {155.8, 155.8}
R <sub>49</sub>	CH + * → CH*	2.35 × 10 <sup>-2</sup>	-0.874	0.0 {0.0, 0.0}
R <sub>50</sub>	CH* → CH + *	3.00 × 10 <sup>13</sup>	0.874	151.2 + $f(T)$ {146.9, 146.9}
R <sub>51</sub>	CH <sub>2</sub> + * → CH <sub>2</sub> *	3.80 × 10 <sup>-2</sup>	-0.162	0.0 {0.0, 0.0}
R <sub>52</sub>	CH <sub>2</sub> * → CH <sub>2</sub> + *	1.86 × 10 <sup>13</sup>	0.162	109.3 + $f(T)$ {104.0, 104.0}
R <sub>53</sub>	CH <sub>3</sub> + * → CH <sub>3</sub> *	1.24 × 10 <sup>-1</sup>	0.244	0.0 {0.0, 0.0}
R <sub>54</sub>	CH <sub>3</sub> * → CH <sub>3</sub> + *	5.72 × 10 <sup>12</sup>	-0.244	42.4 + $f(T)$ {37.1, 37.1}
R <sub>55</sub>	CH <sub>4</sub> + 2* → CH <sub>3</sub> * + H*	2.29 × 10 <sup>-1</sup>	0.788	9.8 + $f(\theta_H, \theta_{CO}, T)$ {16.3, 16.4}
R <sub>56</sub>	CH <sub>3</sub> * + H* → CH <sub>4</sub> + 2*	3.09 × 10 <sup>10</sup>	-0.788	9.4 + $f(\theta_H, \theta_{CO}, T)$ {4.7, 4.6}
R <sub>57</sub>	CH <sub>3</sub> * + * → CH <sub>2</sub> * + H*	3.12 × 10 <sup>11</sup>	0.086	10.6 + $f(\theta_H, \theta_{CO}, T)$ {12.4, 12.4}
R <sub>58</sub>	CH <sub>2</sub> * + H* → CH <sub>3</sub> * + *	3.21 × 10 <sup>10</sup>	-0.086	29.1 + $f(\theta_H, \theta_{CO}, T)$ {25.3, 25.2}
R <sub>59</sub>	CH <sub>2</sub> * + * → CH* + H*	2.75 × 10 <sup>11</sup>	-0.131	20.5 + $f(\theta_H, \theta_{CO}, T)$ {21.9, 21.9}
R <sub>60</sub>	CH* + H* → CH <sub>2</sub> * + *	3.64 × 10 <sup>10</sup>	0.131	23.6 + $f(\theta_H, \theta_{CO}, T)$ {20.3, 20.1}
R <sub>61</sub>	CH* + * → C* + H*	4.58 × 10 <sup>11</sup>	-0.246	27.6 + $f(\theta_H, \theta_{CO}, T)$ {29.1, 29.1}
R <sub>62</sub>	C* + H* → CH* + *	2.18 × 10 <sup>10</sup>	0.246	17.1 + $f(\theta_H, \theta_{CO}, T)$ {13.8, 13.6}
R <sub>63</sub>	CH <sub>3</sub> * + O* → CH <sub>2</sub> * + OH*	7.16 × 10 <sup>10</sup>	0.317	7.1 + $f(\theta_O, \theta_{H_2O}, T)$ {5.4, 6.2}
R <sub>64</sub>	CH <sub>2</sub> * + OH* → CH <sub>3</sub> * + O*	1.40 × 10 <sup>11</sup>	-0.317	35.5 + $f(\theta_O, \theta_{H_2O}, T)$ {24.9, 34.1}

TABLE 1: Continued

no.	reaction	sticking coefficient (unitless) or pre-exponential ( $s^{-1}$ )	temperature exponent $\beta$	activation energy (kcal/mol) and {typical estimates in oxidation zone and reforming zone of CPOX at 1373 K}
CH <sub>4</sub> Oxidation and Reforming on Rh				
R <sub>65</sub>	CH* + OH* → CH <sub>2</sub> * + O*	$1.61 \times 10^{11}$	-0.113	$32.6 + f(\theta_O, \theta_{H_2O}, T)$ {25.5, 31.8}
R <sub>66</sub>	CH <sub>2</sub> * + O* → CH* + OH*	$6.23 \times 10^{10}$	0.113	$19.6 + f(\theta_O, \theta_{H_2O}, T)$ {20.4, 18.3}
R <sub>67</sub>	C* + OH* → CH* + O*	$9.76 \times 10^{10}$	-0.011	$29.8 + f(\theta_O, \theta_{H_2O}, T)$ {22.0, 29.1}
R <sub>68</sub>	CH* + O* → C* + OH*	$1.03 \times 10^{11}$	0.011	$30.4 + f(\theta_O, \theta_{H_2O}, T)$ {30.7, 29.3}
R <sub>69</sub>	CH <sub>2</sub> * + H <sub>2</sub> O* → CH <sub>3</sub> * + OH*	$1.09 \times 10^{11}$	-0.042	$21.3 + f(\theta_O, \theta_{OH}, \theta_{H_2O}, T)$ {39.0, 19.8}
R <sub>70</sub>	CH <sub>3</sub> * + OH* → CH <sub>2</sub> * + H <sub>2</sub> O*	$9.20 \times 10^{10}$	0.042	$5.1 + f(\theta_O, \theta_{OH}, \theta_{H_2O}, T)$ {0.0, 3.9}
R <sub>71</sub>	CH* + H <sub>2</sub> O* → CH <sub>2</sub> * + OH*	$1.28 \times 10^{11}$	0.148	$21.8 + f(\theta_O, \theta_{OH}, \theta_{H_2O}, T)$ {27.4, 20.8}
R <sub>72</sub>	CH <sub>2</sub> * + OH* → CH* + H <sub>2</sub> O*	$7.84 \times 10^{10}$	-0.148	$20.9 + f(\theta_O, \theta_{OH}, \theta_{H_2O}, T)$ {2.9, 19.4}
R <sub>73</sub>	C* + H <sub>2</sub> O* → CH* + OH*	$7.70 \times 10^{10}$	0.260	$17.6 + f(\theta_O, \theta_{OH}, \theta_{H_2O}, T)$ {21.9, 16.6}
R <sub>74</sub>	CH* + OH* → C* + H <sub>2</sub> O*	$1.30 \times 10^{11}$	-0.260	$30.3 + f(\theta_O, \theta_{OH}, \theta_{H_2O}, T)$ {11.1, 28.9}
R <sub>75</sub>	CO* + * → C* + O*	$3.18 \times 10^{11}$	0.654	$49.1 + f(\theta_O, \theta_H, \theta_{CO}, T)$ {56.1, 50.4}
R <sub>76</sub>	C* + O* → CO* + *	$3.15 \times 10^{10}$	-0.654	$12.3 + f(\theta_O, \theta_H, \theta_{CO}, T)$ {0.0, 9.3}
R <sub>77</sub>	CO* + H* → CH* + O*	$6.92 \times 10^{10}$	0.902	$43.2 + f(\theta_H, \theta_O, \theta_{CO}, T)$ {46.8, 42.0}
		$6.92 \times 10^9 d$		
R <sub>78</sub>	CH* + O* → CO* + H*	$1.45 \times 10^{11}$	-0.902	$17 + f(\theta_H, \theta_O, \theta_{CO}, T)$ {5.9, 16.4}
		$1.45 \times 10^{10} d$		
R <sub>79</sub>	CO* + H* → C* + OH*	$7.20 \times 10^{10}$	0.898	$37.7 + f(\theta_H, \theta_O, \theta_{CO}, \theta_{H_2O}, T)$ {49.5, 36.1}
		$7.20 \times 10^9 d$		
R <sub>80</sub>	C* + OH* → CO* + H*	$1.39 \times 10^{11}$	-0.898	$10.9 + f(\theta_H, \theta_O, \theta_{CO}, \theta_{H_2O}, T)$ {0.0, 10.2}
		$1.39 \times 10^{10} c$		
R <sub>81</sub>	2CO* → C* + CO <sub>2</sub> *	$6.48 \times 10^{10}$	0.898	$42.9 + f(\theta_H, \theta_{CO}, T)$ {43.7, 43.1}
R <sub>82</sub>	C* + CO <sub>2</sub> * → 2CO*	$1.54 \times 10^{11}$	-0.898	$0.0 + f(\theta_H, \theta_{CO}, T)$ {0.0, 0.0}
Oxygenates Decomposition on Rh				
R <sub>83</sub>	CH <sub>3</sub> OH + * → CH <sub>3</sub> OH*	$2.94 \times 10^{-1}$	0.633	0.0 {0.0, 0.0}
R <sub>84</sub>	CH <sub>3</sub> OH* → CH <sub>3</sub> OH + *	$2.41 \times 10^{12}$	-0.633	$11.0 + f(T)$ {5.7, 5.7}
R <sub>85</sub>	CH <sub>3</sub> O + * → CH <sub>3</sub> O*	$9.64 \times 10^{-2}$	0.086	0.0 {0.0, 0.0}
R <sub>86</sub>	CH <sub>3</sub> O* → CH <sub>3</sub> O + *	$7.33 \times 10^{12}$	-0.086	$35.2 + f(T)$ {29.9, 29.9}
R <sub>87</sub>	CH <sub>2</sub> O + * → CH <sub>2</sub> O*	$1.82 \times 10^{-2}$	-0.195	0.0 {0.0, 0.0}
R <sub>88</sub>	CH <sub>2</sub> O* → CH <sub>2</sub> O + *	$3.87 \times 10^{13}$	0.195	$22.0 + f(T)$ {16.7, 16.7}
R <sub>89</sub>	HCO + * → HCO*	$3.45 \times 10^{-2}$	-0.885	0.0 {0.0, 0.0}
R <sub>90</sub>	HCO* → HCO + *	$2.05 \times 10^{13}$	0.885	$64.7 + f(T)$ {59.4, 59.4}
R <sub>91</sub>	CH <sub>2</sub> OH + * → CH <sub>2</sub> OH*	$3.45 \times 10^{-2}$	0.189	0.0 {0.0, 0.0}
R <sub>92</sub>	CH <sub>2</sub> OH* → CH <sub>2</sub> OH + *	$2.05 \times 10^{13}$	-0.189	$56.4 + f(T)$ {51.1, 51.1}
R <sub>93</sub>	CH <sub>3</sub> OH* + * → CH <sub>3</sub> O* + H*	$1.47 \times 10^{11}$	0.050	$20.0 + f(\theta_H, \theta_{CO}, T)$ {23.4, 23.6}
R <sub>94</sub>	CH <sub>3</sub> O* + H* → CH <sub>3</sub> OH* + *	$6.80 \times 10^{10}$	-0.050	$2.5 + f(\theta_H, \theta_{CO}, T)$ {0.0, 0.0}
R <sub>95</sub>	CH <sub>3</sub> O* + * → CH <sub>2</sub> O* + H*	$1.03 \times 10^{11}$	0.158	$0.0 + f(\theta_H, \theta_{CO}, T)$ {0.0, 0.0}
R <sub>96</sub>	CH <sub>2</sub> O* + H* → CH <sub>3</sub> O* + *	$9.72 \times 10^{10}$	-0.158	$26.8 + f(\theta_H, \theta_{CO}, T)$ {21.6, 21.4}
R <sub>97</sub>	CH <sub>2</sub> O* + * → HCO* + H*	$2.67 \times 10^{12}$	-0.128	$7.4 + f(\theta_H, \theta_{CO}, T)$ {9.3, 9.3}
R <sub>98</sub>	HCO* + H* → CH <sub>2</sub> O* + *	$3.75 \times 10^9$	0.128	$24.3 + f(\theta_H, \theta_{CO}, T)$ {20.4, 20.2}
R <sub>99</sub>	HCO* + * → CO* + H*	$2.13 \times 10^{11}$	-0.641	$1.7 + f(\theta_H, \theta_{CO}, T)$ {2.7, 2.9}
R <sub>100</sub>	CO* + H* → HCO* + *	$4.71 \times 10^{10}$	0.641	$22.1 + f(\theta_H, \theta_{CO}, T)$ {18.9, 18.6}
R <sub>101</sub>	CH <sub>3</sub> OH* + * → CH <sub>2</sub> OH* + H*	$1.62 \times 10^{11}$	0.275	$9.3 + f(\theta_H, \theta_{CO}, T)$ {11.4, 11.5}
R <sub>102</sub>	CH <sub>2</sub> OH* + H* → CH <sub>3</sub> OH* + *	$6.16 \times 10^{10}$	-0.275	$20.3 + f(\theta_H, \theta_{CO}, T)$ {16.0, 15.9}
R <sub>103</sub>	CH <sub>2</sub> OH* + * → CH <sub>2</sub> O* + H*	$9.25 \times 10^{10}$	-0.062	$9.0 + f(\theta_H, \theta_{CO}, T)$ {9.7, 9.8}
R <sub>104</sub>	CH <sub>2</sub> O* + H* → CH <sub>2</sub> OH* + *	$1.08 \times 10^{11}$	0.062	$7.3 + f(\theta_H, \theta_{CO}, T)$ {3.3, 3.2}

<sup>a</sup> The activation energies are temperature dependent according to statistical mechanics (see Table 2).<sup>8,11</sup> The coverage dependence of the activation energies of various reaction steps is incorporated in our simulations via the UBI-QEP method.<sup>19,20</sup> The functions  $f$  in the last column indicate the nonlinear dependence of activation energies on specific coverages and on temperature. In the last column, numbers in brackets correspond to activation energies in typical CPOX conditions in the oxidation ( $\theta_O \approx 0.7$ ) and reforming ( $\theta_{CH} \approx 0.5$ ,  $\theta_H \approx 0.08$ ,  $\theta_C \approx 0.07$ ,  $\theta_{CH_2} \approx 0.04$ ) zones, at a sample temperature of 1373 K, respectively. Use of submechanisms is recommended depending on the fuel utilized. <sup>b</sup> A bond index of 0.8 is used in the UBI-QEP formula for the calculation of the forward activation energy, instead of the usual value of 0.5 (see ref 11 for details). <sup>c</sup> The backward activation energy is calculated using the forward activation energy of R<sub>9</sub> and the heat of reaction. <sup>d</sup> Optimized pre-exponentials based on SA shown in Figure 3b.

order conservation (BOC) theory).<sup>19,20</sup> UBI-QEP can be thought of as a low level theoretical tool, whose uncertainty in parameter estimation, while typically is 3–5 kcal/mol, could occasionally be substantially larger.  $Q_{CH_3OH}$  is taken from surface science experiments of ref 21, whereas the rest, viz.,  $Q_{CH_3O}$ ,  $Q_{CH_2O}$ ,  $Q_{HCO}$ , and  $Q_{CH_2OH}$ , are taken from the cluster DFT calculations of ref 22. The UBI-QEP method is also used to calculate the activation energies of all surface reaction steps. Many heats of chemisorption and activation energies are coverage dependent due to the adsorbate–adsorbate interactions considered between O\*–O\*, H\*–H\*, OH\*–O\*, H<sub>2</sub>O\*–H<sub>2</sub>O\*, H<sub>2</sub>O\*–OH\*, CO\*–CO\*, and CO\*–H\* (for details on these interactions, see ref 11 and Table 2).

It should be noted that in most cases, closed shell molecules, such as CH<sub>4</sub>, O<sub>2</sub>, H<sub>2</sub>O, etc., participate in reactant adsorption, product desorption, or product readsorption and provide the main means of coupling of gas and surface chemistries. The role of adsorption/desorption of radicals, such as C, CH, etc., is not known a priori. It turns out that most radicals do not play a significant role, given their low mole fractions in the gas-phase and their high surface desorption barriers. Nonetheless, these minor steps provide a convenient basis of linearly independent reactions while ensuring thermodynamic consistency (see below and ref 8), and are therefore included in the C<sub>1</sub> mechanism. Under conditions where gas-phase chemistry may substantially contribute (e.g., high pressures), radicals could be important in



**TABLE 2: Temperature and Coverage-Dependent Heats of Chemisorption Using Statistical Mechanics<sup>8,11</sup> with the UBI-QEP Method<sup>19,20</sup>**

species	heat of chemisorption $Q$ (kcal/mol)	selected refs	temp dependence <sup>b</sup> $(Q(T_0) - Q(T))/R_g\Delta T$	changes in degrees of freedom for deriving the temperature dependence <sup>c</sup>
O*	100 – 21 $\theta_O$	expts, <sup>50–52</sup> DFT <sup>53–55</sup>	1.5	–3F <sub>T</sub> + 3F <sub>V</sub>
CO*	38.5 – 17 $\theta_{CO}$ – 3.7 $\theta_H$	expts, <sup>46,56–58</sup> DFT <sup>11,59,60</sup>	2.0	–3F <sub>T</sub> – 2F <sub>R</sub> + F <sub>RR</sub> + 4F <sub>V</sub>
CO <sub>2</sub> *	5.2	expts, <sup>61,62</sup> UBI-QEP <sup>63</sup>	2.0	–F <sub>T</sub> – 3F <sub>R</sub> + 4F <sub>V</sub>
H*	62.3 – 2.5 $\theta_H$ – 3.7 $\theta_{CO}$	expts, <sup>64</sup> DFT <sup>11,53,65–67</sup>	1.5	–3F <sub>T</sub> + 3F <sub>V</sub>
OH*	70 – 33 $\theta_O$ + 25 $\theta_{H_2O}$	UBI-QEP, <sup>63</sup> DFT <sup>53,66</sup>	2.0	–3F <sub>T</sub> – 2F <sub>R</sub> + F <sub>RR</sub> + 4F <sub>V</sub>
H <sub>2</sub> O*	10.8 – 4.5 $\theta_{H_2O}$ + 25 $\theta_{OH}$	expts, <sup>68</sup> DFT <sup>53,69</sup>	2.5	–3F <sub>T</sub> – 3F <sub>R</sub> + F <sub>RR</sub> + 5F <sub>V</sub>
COOH*	62.2	DFT <sup>17</sup>	2.5	–3F <sub>T</sub> – 3F <sub>R</sub> + F <sub>RR</sub> + 5F <sub>V</sub>
HCOO** (bidentate)	69.2	DFT <sup>17</sup>	3.0	–3F <sub>T</sub> – 3F <sub>R</sub> + 6F <sub>V</sub>
C*	159.0	DFT <sup>17</sup>	1.5	–3F <sub>T</sub> + 3F <sub>V</sub>
CH*	151.2	DFT (this work)	2.0	–3F <sub>T</sub> – 2F <sub>R</sub> + F <sub>RR</sub> + 4F <sub>V</sub>
CH <sub>2</sub> *	109.3	DFT (this work)	2.5	–3F <sub>T</sub> – 3F <sub>R</sub> + F <sub>RR</sub> + 5F <sub>V</sub>
CH <sub>3</sub> *	42.4	DFT <sup>18</sup>	2.5	–3F <sub>T</sub> – 3F <sub>R</sub> + F <sub>RR</sub> + 5F <sub>V</sub>
CH <sub>4</sub>	6.0	expts <sup>16</sup>	2.0	–F <sub>T</sub> – 3F <sub>R</sub> + 4F <sub>V</sub>
CH <sub>3</sub> OH*	11.0	expts <sup>21</sup>	2.5	–3F <sub>T</sub> – 3F <sub>R</sub> + F <sub>RR</sub> + 5F <sub>V</sub>
CH <sub>3</sub> O*	35.2	DFT <sup>22</sup>	2.5	–3F <sub>T</sub> – 3F <sub>R</sub> + F <sub>RR</sub> + 5F <sub>V</sub>
CH <sub>2</sub> O*	22.0	DFT <sup>22</sup>	2.5	–3F <sub>T</sub> – 3F <sub>R</sub> + F <sub>RR</sub> + 5F <sub>V</sub>
HCO*	64.7	DFT <sup>22</sup>	2.5	–3F <sub>T</sub> – 3F <sub>R</sub> + F <sub>RR</sub> + 5F <sub>V</sub>
CH <sub>2</sub> OH*	56.4	DFT <sup>22</sup>	2.5	–3F <sub>T</sub> – 3F <sub>R</sub> + F <sub>RR</sub> + 5F <sub>V</sub>

<sup>a</sup> The heat of chemisorption,  $Q(T)$ , decreases with increasing temperature (here  $\Delta T = T - T_0$  and  $T_0 = 300$  K). <sup>b</sup> The generalized assumptions to calculate the temperature dependence are as follows: (1) Each translational, rotational, and vibrational degree of freedom (DOF) corresponds to  $0.5R_gT$ ,  $0.5R_gT$ , and  $R_gT$ , respectively, where  $R_g$  is the universal gas constant. (2) Upon adsorption, all translational DOF are converted into vibrational DOF. In the case of weakly bound molecules (such as CO<sub>2</sub> and CH<sub>4</sub>), only one translational DOF is lost upon adsorption (the molecule is able to move readily on the surface). (3) All rotational DOF are converted into vibrational DOF upon adsorption. For species, such as OH\*, H<sub>2</sub>O\*, etc., with a vertical axis through the adsorbed atom, 1 of the gained vibrational DOF is assumed to be a free, internal rotor (rigid rotor approximation) and counts as  $0.5R_gT$ . <sup>c</sup> F<sub>T</sub>, F<sub>R</sub>, and F<sub>V</sub> stand for translational, rotational, and vibrational DOF. F<sub>RR</sub> indicates that a vibrational DOF is assumed to be a free, internal rotor. The “minus” and “plus” signs indicate loss and gain of DOF, respectively.

radical recombination and flame quenching studies (see the section on analysis of CPOX process at high pressures).

Using the UBI-QEP method to estimate the activation energies automatically ensures enthalpic consistency at only one temperature. Therefore, we incorporate temperature dependence in the heats of chemisorption by employing statistical mechanics to account for the changes in the degrees of freedom upon adsorption following refs 8 and 11. The formulas are summarized in Table 2. Such temperature dependence makes the activation energies temperature dependent as well. The last column of Table 1 shows an example from the CPOX process to indicate that some of the activation energies change drastically with varying operating conditions or reactor length, due mainly to their coverage dependence. Entropic consistency is ensured in the mechanism by minimizing the deviation between the gas-phase reaction entropies and surface reaction entropies (see refs 8 and 11 for details). It should be noted that *no* experimental data fitting is carried out while making the new subset of the C<sub>1</sub> mechanism thermodynamically consistent, i.e., first the mechanism is made thermodynamically consistent by setting  $w_y = 0$  according to eq 14 of ref 8 (though this task could be done in conjunction with parameter optimization against experimental data). The outcomes of entropic consistency are the values of pre-exponentials (A) and temperature exponents ( $\beta$ ) of the thermodynamically consistent C<sub>1</sub> mechanism.

### Hierarchical Multiscale Parameter Refinement

**Overall Approach for Mechanism Development.** The overall hierarchical mechanism development approach is illustrated in Figure 1b. Semiempirical techniques are used to compute activation energies and order of magnitude TST estimates are employed for pre-exponentials (left top corner of Figure 1b). Thermodynamic consistency is then ensured in the parameters using gas-phase thermodynamics, without any optimization against experimental data.<sup>8</sup> Reaction rates are determined using the mean field approximation (left middle part

of Figure 1b) and are passed into a suitable, simple pseudohomogeneous reactor model (bottom left part of Figure 1b), such as a fixed bed reactor, using the surface Chemkin framework<sup>23</sup> wrapped with user-developed codes.

The next step is to run this model to identify its important or active parameters that strongly control model predictions and assess their uncertainty. Higher level modeling tools can then be used (right part of Figure 1b) to improve the accuracy of these important parameters only, rather than estimating all parameters of a complex model. Sensitivity analysis (SA) is a key tool in identifying the important parameters for each experiment. Diversity in experiments and operating conditions is also essential to increase the number of important parameters. Typically, low-pressure experiments are used for mechanism development to avoid complications of gas-phase chemistry and transport, whereas moderate to high-pressure experiments are utilized for parameter validation.

Herein we use the mean field assumption and simple reactor models and focus on hierarchical multiscale refinement of the reaction parameters using DFT (top right part of Figure 1b). Examples of complex computational fluid dynamics (CFD) models and kinetic Monte Carlo simulations that overcome the mean field approximation (bottom and middle parts of Figure 1b) have been illustrated in previous work.<sup>9,24</sup>

The proposed methodology for parameter refinement is as follows. First SA with respect to the heats of chemisorption is carried out. This is the most critical input into the UBI-QEP method. Identified heats of chemisorption that are important but uncertain are refined using DFT and the runs are repeated. Surface coverages are then analyzed to determine the dominant surface species. Adsorbate–adsorbate interactions between dominant species, which could be between the same (self-interactions) or different (cross-interactions) species that have not been included are estimated using DFT. Since only a couple of species are usually dominant, this dramatically reduces the computational cost associated with performing DFT for all

**TABLE 3: List of Experimental Data Used for either Model Parameter Refinement or Model Validation of the C<sub>1</sub> Mechanism Subsets Depicted in Table 1**

reactant or process	type of experiment or reactor	catalyst type	no. of exptl sets	parameter(s) examined	model response(s)	refs
O <sub>2</sub>	TPD <sup>a</sup>	Rh(111) single crystal	1	temperature, coverage	O <sub>2</sub> desorption rate	51
CO	ignition	Rh/SiO <sub>2</sub> wafer	1	composition	CO ignition temp	70
CO	molecular beam	polycrystalline Rh foil, Rh(111) single crystal	2	temperature, composition	CO <sub>2</sub> production rate	71, 72
CO	TPR <sup>b</sup>	Rh(111) single crystal	1	temperature, coverage	CO and CO <sub>2</sub> desorption rates	73
CO	TPD	Rh(111) single crystal	1	temperature, coverage	CO desorption rate	74
H <sub>2</sub>	ignition	polycrystalline Rh foil	1	composition	H <sub>2</sub> ignition temperature	11
H <sub>2</sub>	LIF	polycrystalline Rh foil	1	temperature	OH mole fraction	75
H <sub>2</sub>	TPR	Rh(100) single crystal	1	temperature	H <sub>2</sub> and H <sub>2</sub> O desorption rates	76
H <sub>2</sub>	TPD	Rh(111) and Rh(100) single crystals	3	temperature, coverage	H <sub>2</sub> desorption rate	64, 77–79
H <sub>2</sub> O	TPD	Rh(111) single crystal	1	temperature	H <sub>2</sub> O desorption rate	80
WGS	fixed bed	Rh/TiO <sub>2</sub>	1	temperature	CO conversion	81
PROX	fixed bed	Rh/MgO	1	temperature	CO conversion, CO <sub>2</sub> selectivity	82
methanation	fixed bed	Rh/TiO <sub>2</sub>	1	composition, temperature	CH <sub>4</sub> production rate	83
CH <sub>4</sub> CPOX	microstructured honeycomb, monolith, microlith	Rh, Rh/alumina	4	pressure, composition, temperature, dilution, flow rate	CH <sub>4</sub> conversion, CO and H <sub>2</sub> selectivities	26, 31, 47–49
CH <sub>4</sub> CPOX	fluidized bed	Rh/alumina	1	composition, temperature, flow rate, air vs O <sub>2</sub> feed	CH <sub>4</sub> conversion, CO and H <sub>2</sub> selectivities	41
autothermal reforming	fluidized bed	Rh/alumina	1	inlet steam composition	CH <sub>4</sub> conversion and CO selectivity	41
CO <sub>2</sub> reforming	fixed bed	Rh/La <sub>2</sub> O <sub>3</sub>	1	temperature	CH <sub>4</sub> and CO <sub>2</sub> conversion	43
CH <sub>3</sub> OH dec	LIF	polycrystalline Rh foil	1	pressure, temperature	CO partial pressure	44
HCHO dec	LIF	polycrystalline Rh foil	1	pressure, temperature	CO production rate	45

<sup>a</sup> Temperature programmed desorption. <sup>b</sup> Temperature programmed reaction.

combinations of species and coverages. In other work, we have also carried out SA with respect to activation energies. DFT-based linear free energy relationships have been employed to improve the bond index of surface reactions (for an example of this idea, see ref 25). Finally, SA with respect to pre-exponentials is carried out to determine the most important reactions. Only those pre-exponentials are tuned within a small uncertainty range against experimental data. It is important that one selects targeted experiments that isolate the important parameters and leave redundant experiments for model validation.

The proposed hierarchical approach is powerful because the total number of refined parameters typically lies between 1 and 5 and is seldom more than 5–10. Since only the important parameters are refined, albeit using CPU intensive applications, this approach is very efficient. It should be noted that mechanism predictions are quantitative in most cases, but a rigorous optimization is avoided, whenever possible, to increase the model fidelity for future refinement, especially as one keeps building mechanisms of more complex fuels (see Figure 1a).

**Need for Parameter Refinement of C<sub>1</sub> Mechanism.** Table 3 summarizes the list of various experimental data considered in the mechanism development and validation. In this section, we discuss the CPOX data that is used for the development of the C<sub>1</sub> mechanism. Other data have been left for validation. Fichtner et al. performed a set of CPOX experiments in a microstructured honeycomb Rh reactor and measured CH<sub>4</sub> conversion and syngas selectivity as a function of pressure.<sup>26</sup> These particular experiments are chosen for mechanism development, since the entire microreactor is made of Rh, thus eliminating the complexities of internal mass transfer. Furthermore, the high thermal conductivity of Rh contributes to a good heat distribution in the flow direction to minimize the temperature gradients that are of the order of 50–120 °C from inlet to

outlet, significantly less than those in ceramic-based monoliths. Last, these operating conditions closely resemble high-pressure, industrially relevant conditions.

The microreactor is modeled as a plug flow reactor (PFR) using the C<sub>1</sub> mechanism. External mass transfer is not found to be important based on the ratios of reaction rate to diffusion rate. Figure 2 shows the predictions for H<sub>2</sub> selectivity as a function of the operating pressure. It should be noted that at such high pressures (10–120 bar), gas-phase chemistry can play a significant role, and hence, the GRI-mech 3.0 mechanism<sup>27</sup> is employed along with the surface chemistry in all high-pressure (> 1 atm) simulations. The predictions are not affected even if the oxygenate decomposition steps (R<sub>83</sub>–R<sub>104</sub>) are eliminated from the simulations. Even though the predicted CH<sub>4</sub> conversion and CO selectivity are qualitatively reasonable (not shown), the H<sub>2</sub> selectivity is significantly underpredicted as shown in Figure 2. This indicates that there is a need to refine the parameters of the C<sub>1</sub> mechanism. Possible causes for this underprediction are poor input in terms of heats of chemisorption, lack of some critical adsorbate–adsorbate interactions, use of crude TST-based pre-exponentials, etc. We explore these causes next.

#### Identification and Refinement of Important Parameters.

According to the hierarchical approach for mechanism development, only the important parameters should be refined. We prefer to fix the energetics first, followed by the pre-exponentials, since the former depend more strongly on adsorbate–adsorbate interactions and affect the reaction rates more crucially. To identify the important parameters, first we perform SA with respect to the heats of chemisorption (*Q*). The model responses (observables) include CH<sub>4</sub> conversion, CO selectivity, and H<sub>2</sub> selectivity. Figure 3a shows the sensitivity coefficients for H<sub>2</sub> selectivity as a model response at 10 and 120 bar (operating conditions corresponding to Figure 2). It is observed that *Q*<sub>CH</sub> and *Q*<sub>CH<sub>2</sub></sub> are the most important parameters. CH<sub>4</sub>

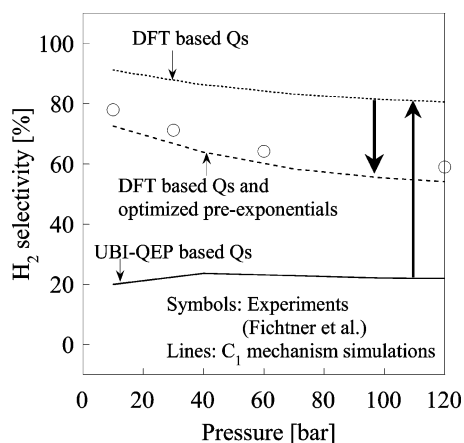


**Figure 2.** Hierarchical improvement in  $\text{H}_2$  selectivity predictions using our  $\text{C}_1$  mechanism against the Rh honeycomb microreactor experiments of ref 26. The operating conditions include a temperature of 1200 °C, a reactor volume of  $\sim 0.05 \text{ cm}^3$ , a reactor length of 0.5 cm, a catalyst area of  $16.2 \text{ cm}^2$ , and an inlet GHSV of  $1.17 \times 10^6 \text{ h}^{-1}$  at STP (note that the inlet velocity changes with temperature and pressure). The inlet composition is 60%  $\text{CH}_4$ , 30%  $\text{O}_2$ , and 10% Ar. The GRI mech. 3.0 mechanism<sup>27</sup> is used along with the surface chemistry. Solid lines indicate the predictions of the  $\text{C}_1$  mechanism with UBI-QEP based heats of chemisorption ( $Q$ ) for CH and  $\text{CH}_2$ . Predictions with DFT-based  $Q_{\text{CH}}$  and  $Q_{\text{CH}_2}$  are shown with dotted lines, whereas dashed lines represent the predictions using DFT-based  $Q_{\text{CH}}$  and  $Q_{\text{CH}_2}$  as well as modified pre-exponentials for  $R_{77}$ – $R_{80}$ . Thick arrows indicate the iterative improvement in mechanism predictions.

conversion shows a similar sensitivity (not shown), whereas CO selectivity depends on these heats of chemisorption at high pressures only (not shown). As mentioned previously,  $Q_{\text{CH}}$  and  $Q_{\text{CH}_2}$  values were estimated using the semiempirical UBI-QEP method, whose uncertainty for radicals could be significant.

Following the SA in Figure 3a, quantum mechanical, periodic DFT calculations are carried out on a three layer  $2 \times 2$  Rh-(111) slab to estimate  $Q_{\text{CH}}$  and  $Q_{\text{CH}_2}$ . Since other  $Q$  values are primarily taken from DFT or surface science experiments, they are left unmodified. The DACAPO software<sup>28</sup> is employed for the DFT calculations. The top two layers of the Rh slab and the adsorbate are relaxed, whereas the bottom layer is fixed. A plane wave basis set with an energy cutoff of 350 eV is employed with an 18 k-point Chadi–Cohen mesh. The PW91 exchange–correlation functional is applied and the Vanderbilt ultrasoft pseudopotential<sup>29</sup> is used to describe the core electrons. It is found that the DFT-based  $Q_{\text{CH}}$  and  $Q_{\text{CH}_2}$  are significantly different from the UBI-QEP based ones. For CH, the DFT estimate is 151.2 kcal/mol compared to the UBI-QEP estimate of 105.5 kcal/mol. Similarly, the DFT estimate for  $\text{CH}_2$  is 109.3 kcal/mol compared to the UBI-QEP estimate of 74.2 kcal/mol. Replacing the UBI-QEP-based  $Q$  values with DFT-based ones in the  $\text{C}_1$  mechanism significantly increases the  $\text{H}_2$  selectivity at all pressures (10–120 bar), as shown in Figure 2. Even though there is a significant improvement in the mechanism reactivity, the simulations now overpredict the model responses.

Since the important  $Q$  values have been corrected using DFT, next possible optimization parameters are the pre-exponentials. A pairwise brute force SA is carried out to identify the most important pre-exponentials of the  $\text{C}_1$  mechanism (with DFT-based  $Q_{\text{CH}}$  and  $Q_{\text{CH}_2}$ ). In pairwise SA, pre-exponentials of the forward and backward reactions are perturbed by the same factor, so that the equilibrium constant is unaffected and thermodynamic consistency is maintained. Figure 3b shows the most important reactions in controlling the  $\text{H}_2$  selectivity at 120

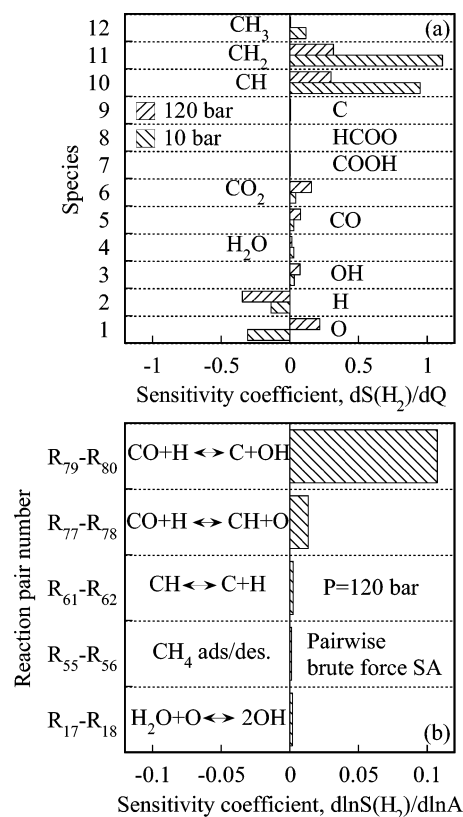
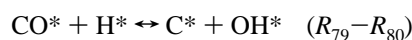
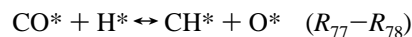


**Figure 3.** Panel a shows brute force SA coefficients for  $\text{H}_2$  selectivity with respect to species heats of chemisorption ( $Q$ ) for conditions of Figure 2. The  $\text{C}_1$  mechanism with UBI-QEP-based  $Q_{\text{CH}}$  and  $Q_{\text{CH}_2}$  is employed. Panel b shows the pairwise brute force SA coefficients for the same conditions for the  $\text{H}_2$  selectivity with respect to pre-exponentials. The  $\text{C}_1$  mechanism with DFT-based  $Q_{\text{CH}}$  and  $Q_{\text{CH}_2}$  is used in these simulations.

bar, for the operating conditions of Figure 2. The most important reactions are



and



Only the important pre-exponentials ( $R_{77}$ – $R_{80}$ ) are decreased by a factor of 10 to improve the mechanism predictions (rigorous optimization is not carried out given the uncertainty in temperature gradients and reactor models). Such an adjustment is well within the uncertainty of pre-exponential ranges for surface reactions. These crudely optimized pre-exponentials of the  $\text{C}_1$  mechanism are shown in italics in Table 1.

Predictions using the  $\text{C}_1$  mechanism with DFT-based  $Q_{\text{CH}}$  and  $Q_{\text{CH}_2}$  and modified pre-exponentials for  $R_{77}$ – $R_{80}$  are also shown in Figure 2. It is evident that there is a significant improvement in the agreement between experiments and simulations for  $\text{H}_2$  selectivity. Figure 4 shows all three model responses, viz.,  $\text{CH}_4$  conversion, CO selectivity, and  $\text{H}_2$  selectivity with surface chemistry alone and combined surface and gas-phase chemistries. Predicted model responses are in reasonable agreement with the experimental data. It is evident that the gas-phase chemistry is important at high pressures ( $>40$  bar), especially for the CO selectivity predictions. To confirm that the decrease in CO selectivity with respect to pressure is not a peculiarity of the GRI-mech 3.0 mechanism, we have also used the Marinov et al. gas-phase reaction mechanism.<sup>30</sup> The predic-

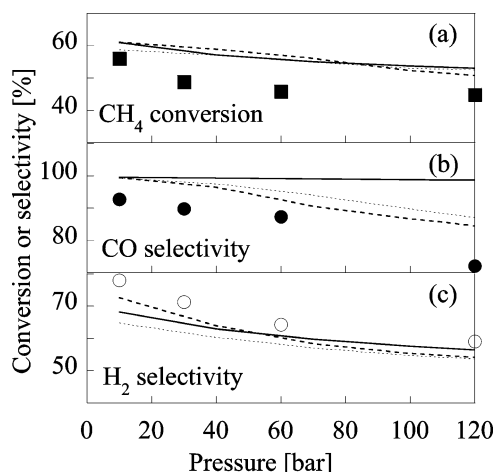


**Figure 4.** Performance of the  $C_1$  mechanism against the Rh honeycomb microreactor experiments of ref 26. The operating conditions are those used in Figure 2. Solid lines correspond to the simulations using surface chemistry only. Simulations (GRI mech. 3.0 mechanism,<sup>27</sup> shown by dashed lines, and Marinov et al. mechanism,<sup>30</sup> shown by dotted lines) indicate that the gas-phase chemistry plays an important role at high pressures.

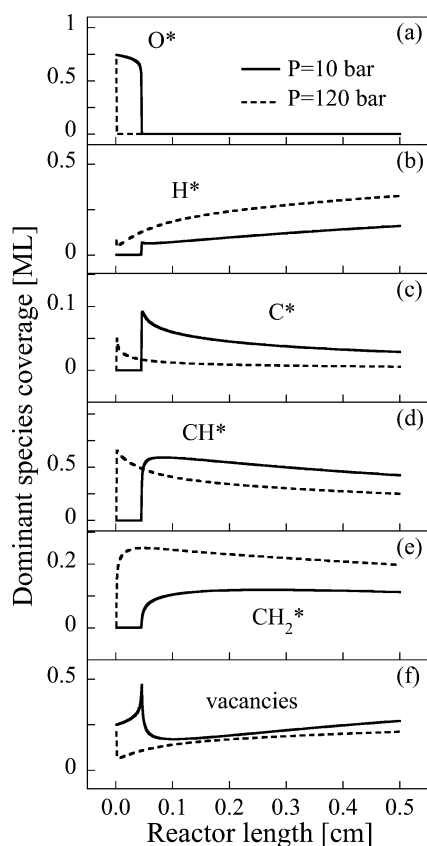


**Figure 5.** Surface coverages of dominant species at 10 and 120 bar, for conditions of Figure 2.  $O^*$  and  $CH^*$  are the dominant species in different spatial regions.

tions in both cases are close, indicating that the gas-phase chemistry is indeed important at high pressures.

Another important step in our hierarchical approach is to include adsorbate–adsorbate interactions between the dominant surface species. This is typically done before any pre-exponential modification. We have checked the dominant surface coverages as a function of reactor length, as shown in Figure 5, at 10 and 120 bar. In the initial part of the reactor,  $O^*$  is the dominant species. After some distance from the entrance, the  $O^*$  coverage

drastically decreases and  $CH^*$  dominates on the surface.  $O^*–O^*$  interactions are considered in the  $C_1$  mechanism (see Tables 1 and 2), but  $CH^*–CH^*$  are not. Our periodic DFT calculations show that  $CH^*–CH^*$  repulsive interactions are  $\sim 13.8$  (kcal/mol)/ML. Including these interactions in the simulations and decreasing the pre-exponentials of  $R_{77}–R_{80}$  by an additional factor of 2 give similar results as without the interactions. Since these interactions are small compared to the heat of chemisorption of 151.2 kcal/mol and they do not affect the model trends, the  $CH^*–CH^*$  interactions are not included further in this work.

The  $C_1$  mechanism is validated against additional sets of experiments carried out in Rh metallic honeycomb, ceramic monoliths, fluidized beds, and fixed beds, and for various inlet compositions, temperatures, flow rates, dilution conditions, autothermal reforming,  $CO_2$  reforming, and thermal decomposition of oxygenates (see Table 3), as shown in the next sections and the Appendix. The  $C_1$  mechanism predicts all these experimental data fairly well, with an exception of some overprediction of CO selectivity in the Rh honeycomb reactor at atmospheric pressure, as addressed in the Appendix (see Figure 4 and Figure 17). The subsets of the  $C_1$  mechanism, viz., CO oxidation,  $H_2$  oxidation, and CO– $H_2$  coupling, have previously been validated against multiple low- to moderate-pressure experiments.<sup>11</sup> CO methanation is also captured qualitatively (not shown). It should be noted that in the development of the  $C_1$  mechanism on Rh, *only two* pre-exponentials of the  $CH_4$  subset are crudely tuned to capture the experimental data and the reverse ones are perturbed by the same factor to ensure thermodynamic consistency.

Finally, it should be noted that in building the  $C_1$  reaction mechanism we have relied on lower reaction subsets without reoptimizing them. It is clear that some of the fundamental hydrogen and carbon monoxide oxidation chemistry (bottom subsets in chemical hierarchy) affects methane experiments (upper subset). The reverse could also be true; e.g., the  $C_1$  subset could affect lower level reactions especially when multiple chemicals are present, such as in WGS and PROX reactions, but this issue has not been explored at this stage. Such a task will require reevaluation of  $\sim 30$  sets of experiments and the possible reoptimization of parameters, a relatively demanding task that we leave for future work. This coupling between subsets becomes an issue as the dividing line of which reaction steps belong to a submechanism is not always sharp and is guided by intuition (a better approach would have been to study the effect of additional reactions in a subset and drop them if found unimportant). Thus, use of corresponding submechanisms is recommended for each fuel utilized. For example, while simulating WGS and PROX experiments, the coupling mechanism ( $R_1–R_{46}$ ) should be employed instead of the entire  $C_1$  mechanism.

### Validation of the $C_1$ Mechanism against High-Pressure, Spatially Resolved CPOX Experimental Data

Lyubovsky et al. carried out methane CPOX experiments in a microlith reactor, with gas sample probes and thermocouples inserted between the screens at multiple locations along the axial direction.<sup>31</sup> The microlith catalytic reactor is made up of a series of discrete, metallic screen substrates, which are coated with a high surface area ceramic washcoat and impregnated with Rh. Species composition and reactor temperature profiles were reported at different pressures ranging from 2 to 8 bar. The experimental data in Figure 6 show that within the first 4–6 mm, oxygen is completely consumed, but methane conversion still increases, possibly due to steam reforming. Additional



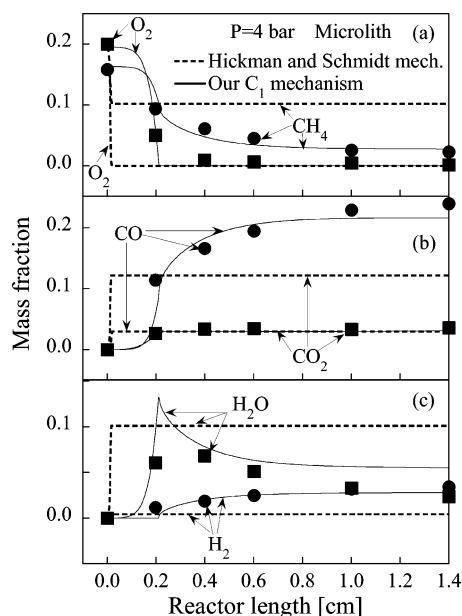


**Figure 6.** Validation of the  $C_1$  mechanism (solid lines) against the microlith reactor experimental data of ref 31 for axial mass fraction profiles of reactants (panel a), C products (panel b), and H products (panel c) and the Hickman and Schmidt mechanism<sup>3</sup> (dashed lines). The GRI mech. 3.0 mechanism<sup>27</sup> is also used. The operating conditions include a pressure of 4 bar, a reactor volume of  $\sim 4.4$  cm<sup>3</sup>, a reactor length of 1.4 cm, an inlet velocity of  $\sim 811.5$  cm/s at STP (note that the inlet velocity changes with temperature and pressure), and an adjusted  $A/V$  of 7500 cm<sup>-1</sup>. The inlet composition is 26% CH<sub>4</sub>, 15.5% O<sub>2</sub>, and 58.5% N<sub>2</sub>. The experimental temperature profile is used in the simulations.

reactions, such as WGS, might also take place under such conditions. This type of experimental data is important in terms of mechanism development or validation, since even though typical reaction mechanisms can possibly predict the exit conversion and/or selectivities, they might not necessarily capture the reaction pathways along the length of the reactor. Furthermore, high-pressure experiments are relevant to practical conditions.

We simulated these experiments as a PFR using the experimental temperature profiles of ref 31 as an input. The Hickman and Schmidt mechanism<sup>3</sup> and the Deutschmann et al. mechanism<sup>32</sup> were also employed. It was found that the Hickman and Schmidt mechanism is highly reactive for oxidation and does not show any reforming, as shown in Figure 6 (dashed lines). Furthermore, the Hickman and Schmidt mechanism does not capture the spatial product profiles. In comparison, the Deutschmann et al. mechanism captures the species profiles fairly well (not shown), upon adjustment of the catalyst area per unit reactor volume ( $A/V$ ) to 1500 cm<sup>-1</sup>. The fact that reforming occurs in the Deutschmann et al. mechanism can qualitatively be inferred from the two-dimensional contour maps reported in ref 33.

Figure 6 also shows simulations using our  $C_1$  mechanism (solid lines) against the high-pressure experiments of Lyubovsky et al.<sup>31</sup> It is evident that the  $C_1$  mechanism is able to capture the axial profiles of major reactants and products very well. It should be noted that only the catalyst area per unit reactor volume ( $A/V$ ) is adjusted to 7500 cm<sup>-1</sup>, a parameter that is not reported, without any optimization of the mechanism parameters. The oxygen consumption location is reasonably well captured. After oxygen is completely consumed, methane conversion keeps increasing, in agreement with the experimental data. Predictions at 2 and 8 bar also show decent agreement with

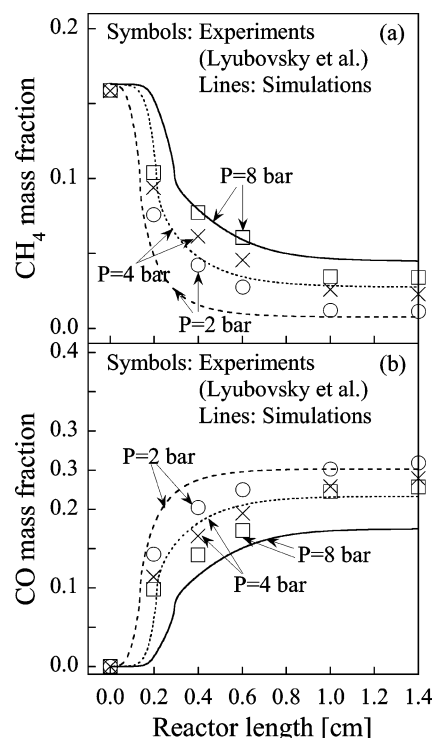


**Figure 7.** Validation of the  $C_1$  mechanism against the microlith reactor experimental data of ref 31 at pressures indicated. The GRI mech. 3.0<sup>27</sup> is also used. The rest of the operating conditions are those of Figure 6. The  $C_1$  mechanism qualitatively captures the spatially resolved data of CH<sub>4</sub> and CO mass fraction profiles.

experiments, as shown in Figure 7. Here we have followed a common strategy employed in gas-phase combustion chemistry modeling, namely, experimental temperature profiles are used as an input to our simulations. This approach bypasses the issue of accurately simulating all heat transfer mechanisms and focuses on the chemistry itself (in principle it eliminates uncertainty propagation from predicting the temperature field into the chemistry). Furthermore, it overcomes the inherent limitation of a PFR model, which does not account for upstream heat transfer.

To our knowledge, this is the first time that a CPOX reaction mechanism has been validated against high-pressure, spatially resolved data. Furthermore, this agreement between experiments and simulations allows us to elucidate the long-standing debate of direct versus indirect methane oxidation,<sup>34</sup> discussed in the next section.

### Analysis of the CPOX Process

In this section, we analyze the high-pressure reaction paths corresponding to simulations of Figure 4 (pressure effects in Rh honeycomb reactor of Fichtner et al.<sup>26</sup>). Similar results hold for the experiments of Lyubovsky et al.<sup>31</sup> as well.

Figure 8 shows the simulated mole fraction profiles for the conditions of Figure 4 at various pressures indicated. Similar to the experiments of Lyubovsky et al.<sup>31</sup> (see Figure 6), oxygen conversion is complete at the front of the reactor, but methane conversion continues to increase. At 10 bar, the decrease in CH<sub>4</sub> and H<sub>2</sub>O mole fractions and the increase in H<sub>2</sub> and CO mole fractions after complete oxygen conversion are indicative of steam reforming. At 120 bar, the CPOX reaction is very fast and occurs very close to the front of the reactor; steam reforming takes over once oxygen is completely consumed. On the basis of the oxygen consumption, the reactor could be divided into

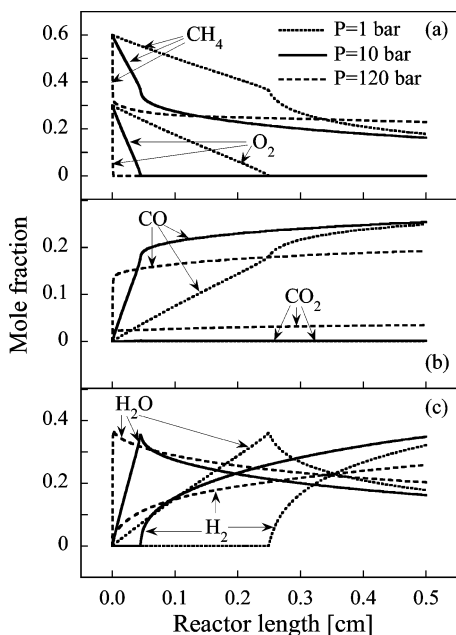


**Figure 8.** Mole fraction profiles using the  $C_1$  mechanism for the conditions of Figure 2. Panels a, b, and c correspond to reactants, C products, and H products, respectively.

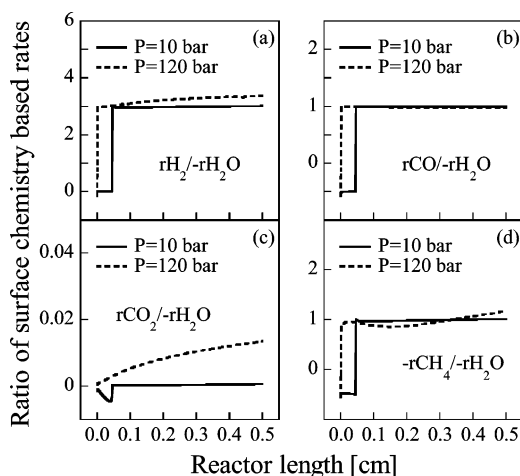
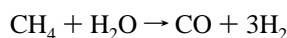


**Figure 9.** Surface chemistry based ratios of rates of species, using the  $C_1$  mechanism, for the conditions of Figure 2 at 10 and 120 bar. At low pressures, methane gets combusted to  $H_2O$  and  $CO$ . Downstream of the oxidation zone, steam reforming takes place. Minor deviations from the steam reforming stoichiometry at 120 bar result from the water–gas shift reaction via gas-phase chemistry.

two regions, viz., an oxidation zone and a reforming zone. The exit  $CO$  mole fraction decreases with increasing pressure. The reverse is true for  $CO_2$ , indicating that WGS reaction could also be contributing along with steam reforming, especially at 120 bar.

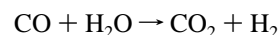
To numerically confirm the steam reforming reaction in the reforming zone, *surface chemistry* based net rates of various species (i.e., desorption minus adsorption) are compared at 10 and 120 bar, as shown in Figure 9. At 10 bar, the ratio of surface rates ( $r^{surf}$ ) of  $CH_4$  consumption to  $H_2O$  consumption ( $-r_{CH_4}^{surf}/r_{H_2O}^{surf}$ , panel d) is initially negative ( $H_2O$  is initially produced) in the oxidation zone, but afterward it approaches 1.0, according to the stoichiometry of the steam reforming reaction



Similarly, the ratios  $r_{CO}^{surf}/-r_{H_2O}^{surf}$  (panel b) and  $r_{H_2}^{surf}/-r_{H_2O}^{surf}$  (panel

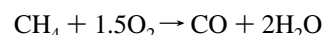
a) approach 1.0 and 3.0, respectively, in agreement with the steam reforming stoichiometry. Furthermore, the ratio  $r_{CO_2}^{surf}/-r_{H_2O}^{surf}$  (panel c) is essentially zero, indicating that no WGS reaction takes place at 10 bar on the surface. Under these conditions, *gas-phase chemistry* is negligibly slow compared to the surface chemistry.

At 120 bar, the ratio of  $H_2$  production to  $H_2O$  consumption ( $r_{H_2}^{surf}/-r_{H_2O}^{surf}$ , panel a) keeps increasing above 3 (3.38 at reactor exit) and the ratio  $r_{CO}^{surf}/-r_{H_2O}^{surf}$  (panel b) keeps decreasing below 1 (0.97 at reactor exit) in the reforming zone. This is a minor deviation from the steam reforming stoichiometry and indicates that WGS could occur simultaneously with steam reforming. This scenario could result in an increase in  $H_2$  moles produced per mole of  $H_2O$  consumed, provided that steam reforming still dominates over WGS. Since steam reforming involves an increase in the number of moles, it is at least thermodynamically less favored at 120 bar compared to 10 bar, according to Le Chatelier's principle. In comparison, WGS with zero net mole change

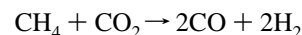


is not pressure dependent. Our simulations indicate lower methane conversion and higher  $H_2O$  mole fraction (lower  $H_2$  selectivity) at 120 bar compared to 10 bar, consistent with slowing down of the steam reforming process. Finally, the presence of  $CO_2$ , and hence the small decrease in  $CO$  selectivity (only  $\sim 1\%$  when only surface chemistry is used, as shown in Figure 4), possibly indicates a *minor* contribution of WGS at 120 bar through surface chemistry. Similar rate comparisons for the ratios  $-r_{CO}^{gas}/-r_{H_2O}^{gas}$  and  $r_{CO_2}^{gas}/-r_{H_2O}^{gas}$  based on the *gas-phase* chemistry agree with the WGS stoichiometry, indicating that WGS *mainly* takes place through the gas-phase at 120 bar and is responsible for the decrease in  $CO$  selectivity ( $\sim 15\%$  when both gas and surface chemistries are used, as shown in Figure 4). Another interesting observation at 120 bar is that some  $C_2$  species ( $\sim 3\%$   $C_2H_4$  and  $\sim 1\%$   $C_2H_6$ ) are also formed in the gas phase. In comparison, the fraction of  $C_2$  species is negligible at 10 bar.

A similar rate comparison confirms (not shown) that  $CO$  and  $H_2O$  are the primary products from the surface in the oxidation zone via the overall reaction



which is a combination of methane CPOX and  $H_2$  oxidation via surface chemistry.  $CO_2$  reforming, given as



is another pathway that could occur. However, a negligible value for the ratio  $-r_{CO_2}^{surf}/-r_{CH_4}^{surf}$  indicates (not shown) that  $CO_2$  reforming is not taking place under these operating conditions, at least via the surface chemistry. On the basis of the gas-phase rate ratio  $-r_{CO_2}^{gas}/-r_{CH_4}^{gas}$ , no definite conclusions could be drawn regarding the gas-phase  $CO_2$  reforming, mainly due to the occurrence of multiple gas-phase reactions involving  $CH_4$  (e.g.,  $C_2$  species production and consumption). Finally, we note that even though Le Chatelier's principle is valid for equilibrium conditions, it provides a consistent explanation for the CPOX conditions analyzed here.

We also carried out reaction path analysis (RPA) to understand the important surface reaction paths. Figure 10 shows only the dominant paths of species production and consumption based on the net rates (forward minus backward) at 10 and 120 bar,

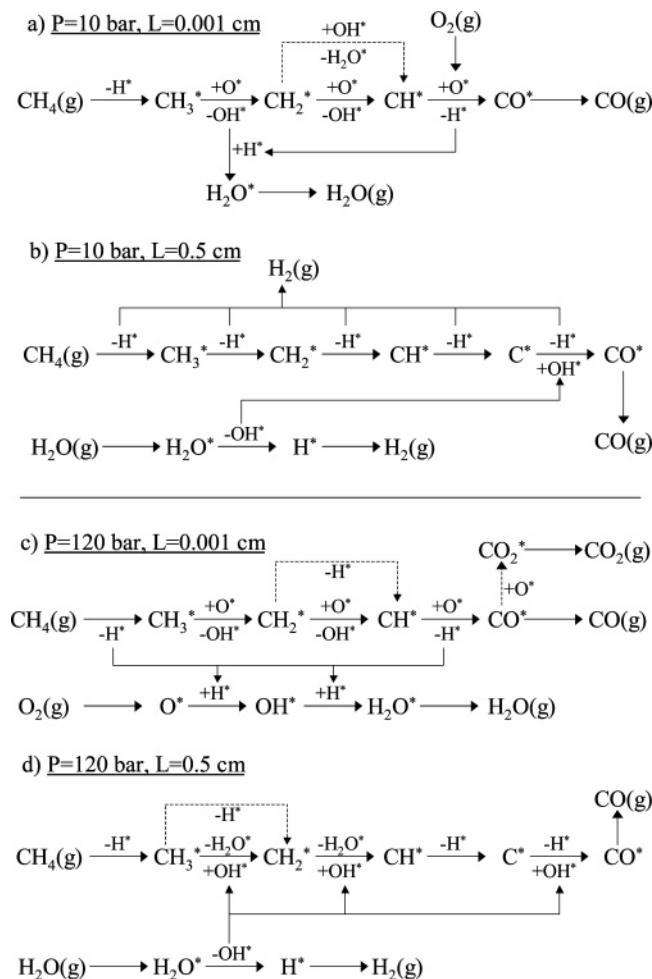


**Figure 10.** Schematic representation of the species production/consumption pathways, using the  $C_1$  mechanism for the conditions of Figure 2 at 10 and 120 bar, in the oxidation zone (at a sample reactor length of 0.001 cm) and reforming zone (at reactor length of 0.5 cm). The most dominant paths are shown with solid lines. Dashed lines indicate alternate, less important but not negligible paths.

in both the oxidation zone (at a sample reactor length of 0.001 cm) and the reforming zone (at a reactor length of 0.5 cm). A main difference between the oxidation and reforming zones at 10 bar is that oxygen is present only in the oxidation zone. As a result,  $\text{CH}_x$  dehydrogenation is mainly oxygen assisted in the oxidation zone, whereas it is primarily thermal in the reforming zone. In the oxidation zone, CO and  $\text{H}_2\text{O}$  are generated as the main gas-phase products.  $\text{CO}^*$  is primarily formed from  $\text{CH}^*$  in the oxidation zone, whereas  $\text{C}^*$  oxidation is the dominant CO formation path in the reforming zone. An interesting observation is that in the reforming zone, it is the  $\text{H}_2\text{O}$  adsorption (water that is formed and desorbed from the oxidation zone) that gives rise to  $\text{H}_2$  production (oxidation of  $\text{C}^*$  via  $\text{OH}^*$  produced by  $\text{H}_2\text{O}^*$  dissociation).  $\text{CO}_2$  formation is insignificant in both zones, as shown in Figure 10 (panels a and b). RPA at 120 bar is different from 10 bar only in that in the oxidation zone, some  $\text{CO}^*$  is oxidized into  $\text{CO}_2^*$  that desorbs (Figure 10c), whereas in the reforming zone, no  $\text{CO}_2^*$  is formed from  $\text{CO}^*$  (Figure 10d). This finding, in conjunction with the experiments of Lyubovsky et al.,<sup>31</sup> clearly indicates that  $\text{CO}_2$  in the reforming zone is produced from CO through *gas-phase* WGS chemistry.

Since  $\text{CO}^*$  is a key intermediate in the mechanism and CO selectivity decreases with increasing pressure, RPA for  $\text{CO}^*$  production has been performed and is shown in Figure 11 at

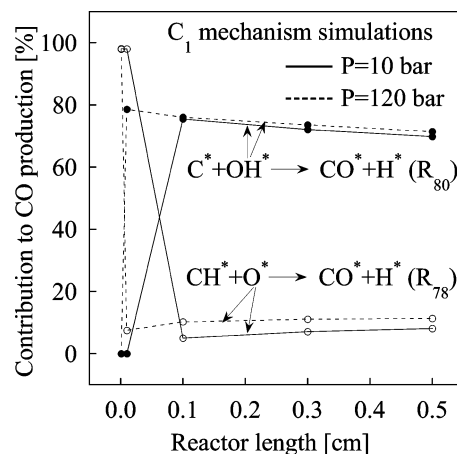
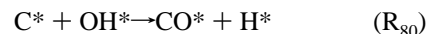
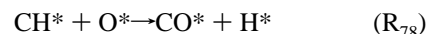


**Figure 11.** Reaction path analysis (RPA) for CO production, using the  $C_1$  mechanism for the conditions of Figure 2. Similar RPA is observed at both pressures (10 and 120 bar), indicating that the decrease in CO selectivity with increasing pressure is associated with the gas-phase chemistry and not the  $C_1$  mechanism.

10 and 120 bar. Under these conditions, the most important  $\text{CO}^*$  production pathways are



and



Even though there is a switch over in the importance of these paths in the oxidation and reforming zones, the dominant reactions are the same and surface chemistry does not play much of a role in lowering the CO selectivity as pressure increases. Similarity in these analyses at all pressures again emphasizes that the surface chemistry is the same at all pressures. The equilibrium limitations of the overall steam reforming reaction and the competition of WGS (in gas-phase) with steam reforming are mainly responsible for the decrease in CO selectivity with increasing pressure. It should be noted that quantitative predictions require proper coupling between the gas-phase and surface chemistries, an issue addressed by the thermodynamically consistent  $C_1$  mechanism presented here.

An interesting question is what is the coupling between gas and surface chemistries. As an example, at 120 bar where gas-phase chemistry is important, the fate of some key radicals ( $\text{H}$ ,  $\text{OH}$ , and  $\text{CH}_3$ ) has been analyzed. Gas-phase RPA along with calculation of the net adsorption/desorption rates of these radicals indicates that ca. one-third of the gaseous  $\text{CH}_3$  radical is produced via surface chemistry (the rest forms from gas-phase  $\text{C}_2$  species decomposition) that plays a role in the formation of  $\text{C}_2$  species in the gas phase. However, only  $\sim 1\%$  of the gaseous  $\text{OH}$  radical is produced from surface chemistry via desorption. This catalyst promotion of gas-phase chemistry is small.  $\text{OH}$  radical in the gas phase primarily attacks CO to produce  $\text{CO}_2$  via  $\text{CO}(\text{g}) + \text{OH}(\text{g}) \rightarrow \text{CO}_2(\text{g}) + \text{H}(\text{g})$ , consistent with our hypothesis of WGS reaction in gas phase. On the other hand, almost all the  $\text{H}$  radical produced in the gas-phase is consumed by surface chemistry (surface induced gas-phase chemistry inhibition). Overall, our simulations indicate that there is some small to moderate coupling between gas and surface chemistries at high pressures mediated via radicals. However, the main coupling appears to arise from sharing reactants and products.

Many research groups have proposed the idea of indirect methane oxidation, in which methane is first oxidized to combustion products followed by reforming that produces syngas. For example, simulations of refs 33 and 35 and continuous flow experiments of ref 36 supported indirect methane oxidation. Other researchers believe that direct methane oxidation takes place, i.e., CPOX products are not formed from combustion products by reforming; instead, depending on the oxygen concentration, CO and H<sub>2</sub> could then be converted into CO<sub>2</sub> and H<sub>2</sub>O, respectively.<sup>37,38</sup> Hofstad et al.<sup>39</sup> have suggested that the primary products are dependent on the surface oxygen available and a support could provide extra oxygen to convert the partial oxidation products into complete oxidation ones. Different conclusions regarding the primary products in methane oxidation indicate that the oxidation paths are still unclear and could be affected by the support state and whether transient or steady state experiments are conducted. Even though we do not explore any support effects in this work, the spatially resolved experiments of Lyubovsky et al.<sup>31</sup> and the simulations using our C<sub>1</sub> mechanism (see Figures 6–11) indicate that in the oxidation zone partial oxidation of methane to CO takes place along with combustion to H<sub>2</sub>O. Once oxygen is completely consumed, steam reforming takes over with a possibility of gas-phase WGS at very high pressures (120 bar) in the reforming zone. Analysis at atmospheric pressure indicates similar inferences as those at 10 bar, the only difference being an increase in the length of the oxidation zone (see Figure 8). Here, we have shown that experiments relevant to industrial conditions can be utilized to assess a predictive microkinetic model and improve our understanding of catalytic methane oxidation and reforming pathways.

Coverages in Figure 5 indicate no coking in the beginning but some as the transition from the oxidation to the reforming zone starts. The C\* coverage decreases downstream due to steam reforming. Under these conditions, the activation energy of the CH\* decomposition to C\* (R<sub>61</sub>) is ~29 kcal/mol, whereas the activation energies of the major C\* consumption paths (R<sub>76</sub> and R<sub>80</sub>) are ~9 and ~10 kcal/mol, resulting in low C\* coverage (the adsorption/desorption steps are not important at 1 atm). As a result, our model predicts CH\* as the dominant carbon-containing species in contrast to previous modeling work on Pt, e.g., ref 40. The predicted dominant CH\* species could be speculated as a hydrogenated precursor leading to coke in the absence of efficient reforming. Realistic modeling of coke formation though would require polymerization type of paths, which are beyond the scope of this work.

### Validation of the C<sub>1</sub> Mechanism against Reforming Experiments

Even though no optimization has been carried out against reforming experiments, the C<sub>1</sub> mechanism could be used for reforming and, hence, it is validated against autothermal and dry reforming experiments in this section.

**Autothermal Reforming of Methane.** Bharadwaj and Schmidt studied the effect of inlet steam on methane oxidation in a fluidized bed reactor.<sup>41</sup> The experimental data are shown in Figure 12a. Using a continuous stirred tank reactor (CSTR) model, we observed that the C<sub>1</sub> mechanism predictions are in good agreement with the experiments. It is observed that the effect of inlet steam (35% in feed) is to increase the CH<sub>4</sub> conversion by ~11% compared to a case where the steam is replaced by N<sub>2</sub>. However, the CO selectivity is significantly decreased (~36%). Our simulations indicate that due to the inlet steam, the H<sub>2</sub>O\* and OH\* coverages increase by an order of

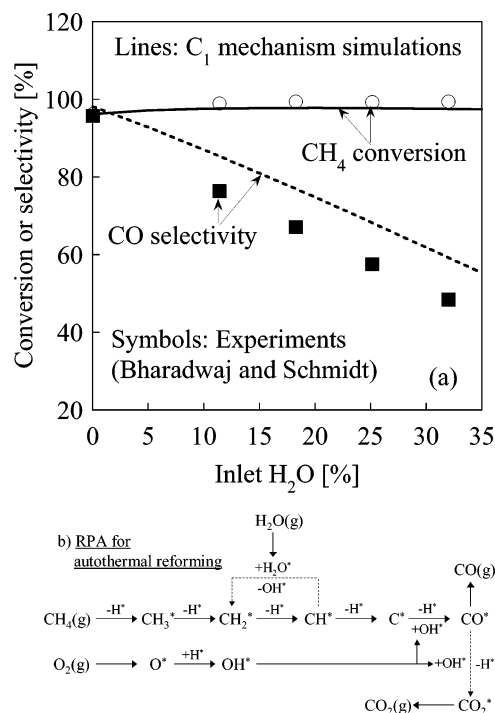
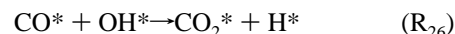


**Figure 12.** Panel a shows the validation of the C<sub>1</sub> mechanism against the autothermal reforming experimental data of ref 41. The operating conditions include a pressure of 1 atm, a reactor volume of ~24.7 cm<sup>3</sup>, a catalyst area of 5.25 × 10<sup>4</sup> cm<sup>2</sup>, an inlet flow rate of 1.2 L/min at STP, and a feed of CH<sub>4</sub>/air. Panel b shows a schematic representation of the species production/consumption pathways. Most dominant paths are shown with solid lines. Dashed lines indicate alternate, less important but non-negligible paths.

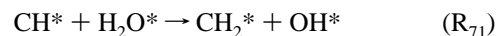
magnitude, which in turn result in an increased rate of the CO–H<sub>2</sub> coupling chemistry, primarily the CO consumption pathways



and



Figure 12b shows that in the presence of steam, increased OH\* production occurs via the reaction



and the rates of CO consumption reactions in the CO–H<sub>2</sub> coupling chemistry (R<sub>26</sub>, R<sub>30</sub>, and R<sub>33</sub>) increase. Since CO is consumed by the coupling chemistry to produce CO<sub>2</sub>, the CO selectivity decreases. This behavior is reminiscent of the promoting role of H<sub>2</sub>O in CO oxidation reported in the ultrahigh vacuum experiments of ref 42 and modeled in ref 10, albeit on Pt. This analysis also indicates that the CO–H<sub>2</sub> coupling chemistry plays an important role in the autothermal reforming of methane.

**CO<sub>2</sub> Reforming of Methane.** Validation is next carried out against the CO<sub>2</sub> reforming experiments of Basini and Sanfilippo.<sup>43</sup> These researchers collected CH<sub>4</sub> and CO<sub>2</sub> reforming data in a fixed bed reactor close to equilibrium conditions, using an Rh/La<sub>2</sub>O<sub>3</sub> catalyst. We simulated these experiments using a fixed bed reactor model, and the predictions are shown in Figure 13a. Since our C<sub>1</sub> mechanism is thermodynamically consistent over a wide temperature range, good agreement is observed with the



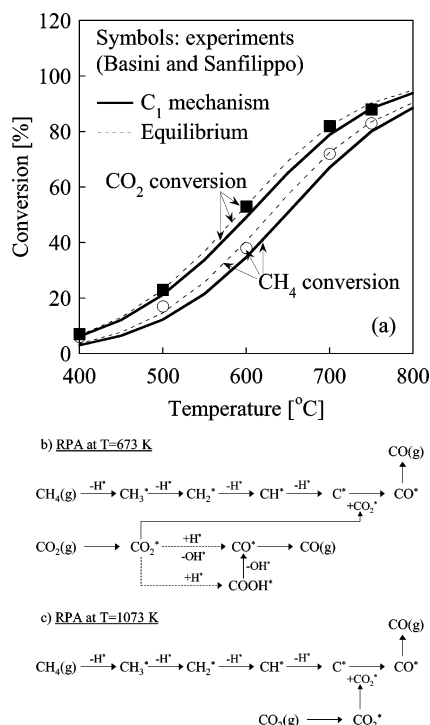
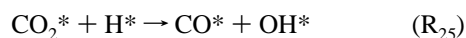


**Figure 13.** Panel a shows validation of the  $C_1$  mechanism against the fixed bed reactor  $CO_2$  reforming experiments of ref 43. The operating conditions include a pressure of 1 bar, a reactor volume of  $\sim 0.7 \text{ cm}^3$ , a reactor length of 1 cm, a catalyst area of  $4 \times 10^4 \text{ cm}^2$ , and GHSV of  $11000 \text{ h}^{-1}$  at  $750^\circ\text{C}$ , and a feed of 1:1  $CH_4/CO_2$ . The experimental data are very close to equilibrium conversions (calculated using the GASEQ software<sup>84</sup>). Panel b shows a schematic representation of the species production/consumption pathways. Most dominant paths are shown with solid lines. Dashed lines indicate alternate paths that are less important but not negligible.

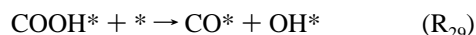
experimental data without any adjustment of the model parameters. In comparison, the Deutschmann et al. mechanism<sup>32</sup> and the Hickman and Schmidt mechanism<sup>3</sup> do not show any activity over the experimental temperature range. Predicted coverages at low (673 K) and high (1073 K) temperatures are shown in Figure 14.  $CH^*$  is the most dominant species at both temperatures under nonequilibrium conditions (short distances). RPA is carried out at both low and high temperatures at the front of the reactor to understand the important reactions in  $CO_2$  reforming under nonequilibrium conditions.  $C^*$  is produced from sequential thermal dehydrogenation of  $CH_4$  at both temperatures, as shown in parts b and c of Figure 13. RPA for  $CO_2$  consumption indicates that there are three main contributing reactions over 673–1073 K, viz.



and



Similarly, RPA for CO production indicates that there are three main contributing reactions, viz.,  $R_{25}$ ,  $R_{82}$ , and



As shown in Figure 13b, at low temperatures, the coupling reactions  $R_{25}$  and  $R_{32}$  along with the reverse Boudouard reaction  $R_{82}$  are responsible for  $CO_2$  consumption. On the other hand,

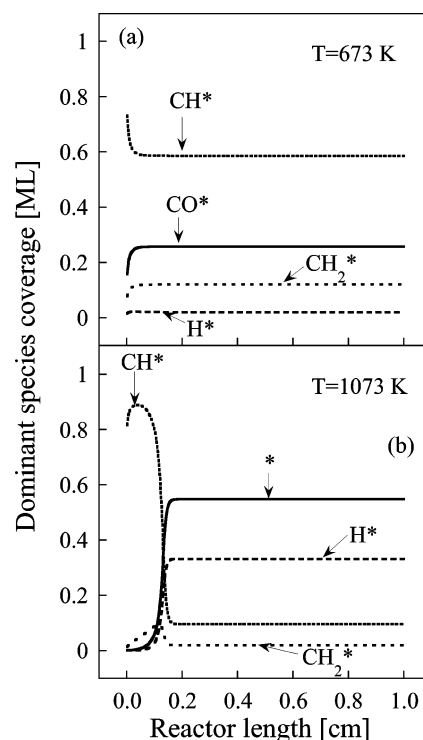


**Figure 14.** Surface coverages of dominant species using the  $C_1$  mechanism, for conditions of Figure 13a at 673 and 1073 K.  $CH^*$  is the dominant species under nonequilibrium conditions. Asterisk indicates vacancies.

at high temperatures, only the reverse Boudouard reaction  $R_{82}$  contributes to  $CO_2$  consumption, as shown in Figure 13c. Similarly, RPA for CO production indicates that at low temperatures, the coupling reactions  $R_{29}$  and  $R_{25}$  are important, whereas at high temperatures, the reverse Boudouard reaction  $R_{82}$  is solely contributing. This is an important result since it emphasizes the necessity of including the  $CO-H_2$  coupling chemistry discussed in ref 11 in modeling dry reforming as well. Other evidence for the role of coupling steps comes from the fact that the literature mechanisms, which do not include these coupling pathways, are relatively inactive for dry reforming of methane.

### Oxygenates Decomposition on Rh

**$C_1$  Mechanism Predictions.** In this section, we compare the performance of the  $C_1$  mechanism (including the oxygenate decomposition steps  $R_{83}$ – $R_{104}$ ) against two oxygenate decomposition experiments. Zum Mallen and Schmidt carried out laser-induced fluorescence (LIF) experiments on a polycrystalline Rh foil to measure the CO partial pressure as a function of temperature.<sup>44</sup> Pure methanol at different total pressures was fed to the reactor. Simulations using the  $C_1$  mechanism are shown in Figure 15a. The onset of activity for CO production, the CO partial pressures, and the composition effects are reasonably well captured by the  $C_1$  mechanism. No parameter adjustment is carried out in these simulations to improve the mechanism performance. Similar experiments were carried out by Papapolymerou and Schmidt using formaldehyde in the inlet.<sup>45</sup> Comparison of simulations using the  $C_1$  mechanism and the experimental data of ref 45 is shown in Figure 16a. In the latter experiment, the rates of CO production are normalized with the experimental data at sample conditions of 0.1 Torr and 1030 K. Good qualitative agreement is observed between simulations and experiments.

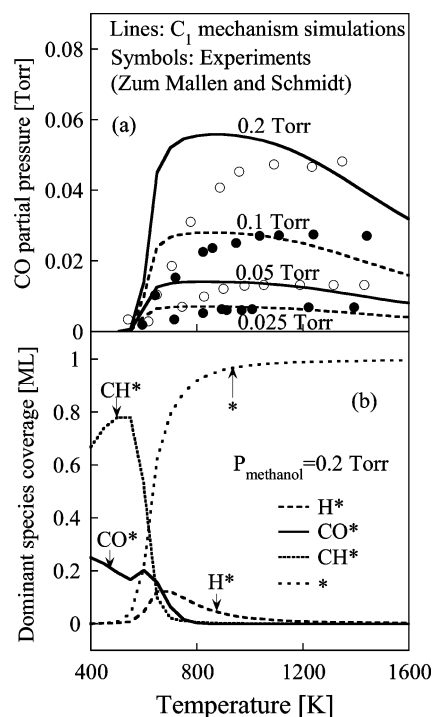
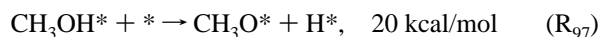
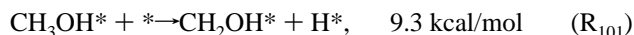


**Figure 15.** Panel a shows the predictions of the  $C_1$  mechanism against the LIF experiments of ref 44. The operating conditions include a reactor volume of 0.4 L, a catalyst foil area of 0.51 cm<sup>2</sup>, and a residence time of 4 s. The inlet consists of pure methanol at four different pressures. Dominant coverages at 0.2 Torr are shown in panel b.

**Analysis of the Mechanism Predictions.** Figure 15b shows the dominant surface coverages for the methanol decomposition experiment (Figure 15a) at 0.2 Torr. CH\* is the dominant species at low temperatures (~400–550 K), where the CO production is not significant. However, at higher temperatures, the surface sites are mostly vacant. We carried out RPA for this experiment at 400 and 600 K. RPA at 400 K shows that adsorbed methanol primarily undergoes desorption (99.998%) and only 0.002% is consumed in CH<sub>2</sub>OH\* production. A relatively negligible percentage of methanol (~10<sup>-9</sup>%) is consumed in the competitive pathway of CH<sub>3</sub>O\* formation. This is due to the significant difference in the activation energies of the two paths



versus



Recent DFT work of Gokhale et al. also shows that C–H bond scission is preferred to O–H bond scission in methanol decomposition on Pt(111).<sup>14</sup>

CH<sub>2</sub>OH\* is then consumed to produce formaldehyde, which in turn is consumed to produce HCO\*. Finally, HCO\* decomposes to form CO\*. Along with CO desorption, CO\* is consumed via R<sub>81</sub> (2CO\* → C\* + CO<sub>2</sub>\*). C\* is then primarily utilized by H\* to produce CH\* via R<sub>62</sub> (C\* + H\* → CH\* + \*), resulting in high CH\* coverage. In comparison, RPA at 600 K shows that more methanol (~1.1%) is consumed to form CH<sub>2</sub>OH\*. CH<sub>3</sub>O\* production is negligible (~10<sup>-4</sup>%). CO desorption significantly increases due to the higher temperature, and more gaseous CO is produced. RPA for the formaldehyde decomposition experiment at sample conditions of 600 K and 0.2 Torr shows similar production–consumption paths for formaldehyde,

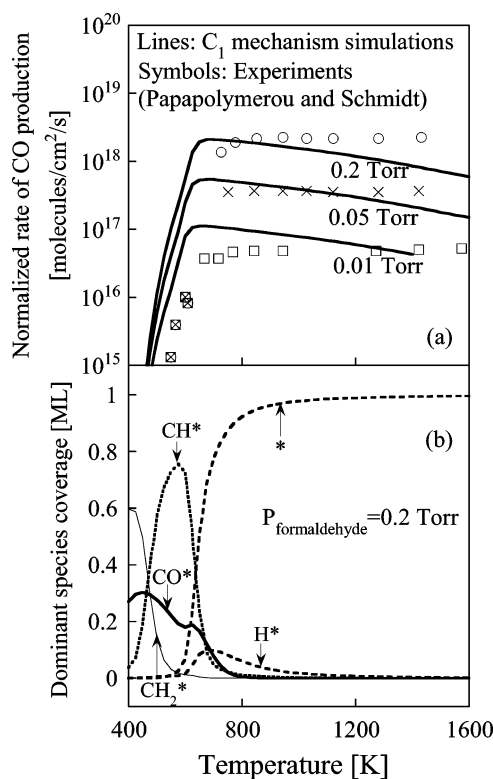
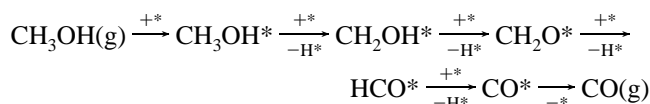


**Figure 16.** Panel a shows the predictions of the  $C_1$  mechanism against the LIF experiments of ref 45. The operating conditions include a reactor volume of 0.4 L, a catalyst wire diameter of 0.019 cm, a catalytic wire length of 9 cm, and a residence time of 4 s. The inlet consists of pure formaldehyde at five different pressures (predictions at 0.1 and 0.02 Torr are not shown for clarity). Model predictions are normalized against the experimental CO production rate at sample conditions of 0.1 Torr and 1030 K. Dominant coverages at 0.2 Torr are shown in panel b.

HCO\*, and CO\*, as in the methanol decomposition simulations. Furthermore, the dominant coverages in Figure 16b show similar trends as in Figure 15b. Overall, the oxygenate decomposition path is given as



The testing of the reaction mechanism presented should be viewed as a first step toward understanding the chemistry of oxygenates. Further experiments and modeling will be necessary to better refine this subset of the  $C_1$  mechanism.

## Conclusions

By use of a hierarchical multiscale modeling approach, a  $C_1$  mechanism is developed on Rh. The rate parameters are estimated from experimental data, semiempirical methods, and first-principles techniques. Thermodynamic consistency is ensured in the rate parameters. A hierarchical parameter refinement is demonstrated using sensitivity analysis followed by density functional theory calculations. With an adjustment of *only two* pre-exponentials of the CH<sub>4</sub> oxidation subset, the  $C_1$  mechanism is shown to capture well different partial oxidation and reforming experiments of methane and the thermal decomposition of oxygenates. A comparison with spatially resolved data is presented, under industrially relevant operating conditions of high pressures. An oxidation zone is predicted to exist in the

front of the reactor, followed by a reforming zone. CO and H<sub>2</sub>O are the primary products in the oxidation zone, indicating that methane oxidation in the presence of oxygen goes through a combination of partial *and* complete oxidation reactions ( $\text{CH}_4 + 1.5\text{O}_2 \rightarrow \text{CO} + 2\text{H}_2\text{O}$ ). The water produced upstream is adsorbed in the reforming zone to drive steam reforming ( $\text{CH}_4 + \text{H}_2\text{O} \rightarrow \text{CO} + 3\text{H}_2$ ) and produce H<sub>2</sub>. It is also shown that the water–gas shift reaction in the gas-phase could play a significant role at high pressures (>40 bar) in decreasing the CO selectivity. Given the increasing importance of syngas production and the high performance of Rh as a CPOX catalyst, the proposed C<sub>1</sub> mechanism could hopefully assist in the understanding and design of methane oxidation and reforming processes. Use of these mechanism in reactor design and scale up will obviously need a careful examination of transport phenomena and fluid dynamics, as depicted in Figure 1b. Reaction subsets developed using the proposed hierarchical approach can be found electronically at ref 85.

**Acknowledgment.** This work was supported in part by ConocoPhillips and by the donors of the Petroleum Research Fund, administered by the American Chemical Society.

#### Appendix: Additional Validation of the C<sub>1</sub> Mechanism against Atmospheric Pressure CPOX Data

**Predictions against Rh Metallic Honeycomb Microreactor Data.** Along with the pressure effects shown in Figure 4, Fichtner et al. performed CPOX experiments in the microstructured honeycomb Rh reactor to measure CH<sub>4</sub> conversion and syngas selectivity as a function of temperature.<sup>26</sup> Predictions using the C<sub>1</sub> mechanism with a PFR model are shown in Figure 17. The temperature effects on all model responses are reasonably well captured by the C<sub>1</sub> mechanism. The CO selectivity is overpredicted by ~10–15%. SA with respect to the heats of chemisorption (*Q*) shows that *Q*<sub>CO</sub> is the most important parameter. Therefore, the overprediction could mainly be due to using the same value of *Q*<sub>CO</sub> for all the experiments involving different types of catalysts. A summary of experimental *Q*<sub>CO</sub> on different catalyst facets is given in ref 46. *Q*<sub>CO</sub> varies from ~31 to ~42 kcal/mol. DFT-based values show strong CO binding up to ~46 kcal/mol.<sup>17</sup> Since we have considered an intermediate value of *Q*<sub>CO</sub> in ref 11, which is not modified here, the agreement for CO selectivity in Figure 17 is considered to be adequate. Uncertainty in the experimental measurements, temperature gradients, and the simplicity of reactor model could be alternative reasons for the discrepancy.

**Predictions against Ceramic Monolith Reactor Data.** Tornaiainen et al. carried out CH<sub>4</sub> CPOX experiments in a Rh-coated ceramic monolith reactor to measure CH<sub>4</sub> conversion and syngas selectivity as a function of inlet composition with an inlet N<sub>2</sub> mole percent of 3.95% (5% air and 95% CH<sub>4</sub>+O<sub>2</sub>).<sup>47</sup> It should be noted that the downstream temperature reported in those experiments could be significantly less than the reaction temperature with a typical uncertainty of 100–200 °C. Performance of the C<sub>1</sub> mechanism against these experimental data is shown in Figure 18 (panel a), when the reactor temperature is taken to be 75 °C higher than the reported one at the exit. Our PFR simulations show decent agreement with the experiments. It should be noted that even without the temperature modifications, the trends in CH<sub>4</sub> conversion and syngas selectivity are captured by the C<sub>1</sub> mechanism and the predictions are within ~25% of the experimental data. Similar CPOX experiments have been carried out in a monolith by Bodke et al., but with 30% N<sub>2</sub> in the feed.<sup>48,49</sup> Again, good agreement is observed

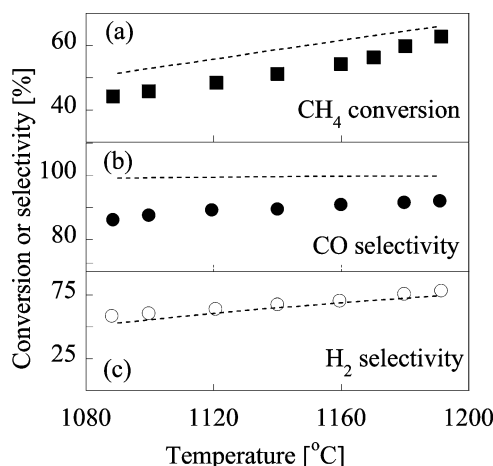


**Figure 17.** Validation of the C<sub>1</sub> mechanism against the Rh honeycomb microreactor experiments of ref 26. Symbols correspond to experimental data, whereas dashed lines indicate model predictions. The operating conditions include a pressure of 1.2 bar, a reactor volume of ~0.05 cm<sup>3</sup>, a reactor length of 0.5 cm, a catalyst area of 16.2 cm<sup>2</sup>, and an inlet GHSV of 780 000 h<sup>-1</sup> at STP (note that the inlet velocity changes with temperature and pressure). The inlet composition is 60% CH<sub>4</sub>, 30% O<sub>2</sub>, and 10% Ar.

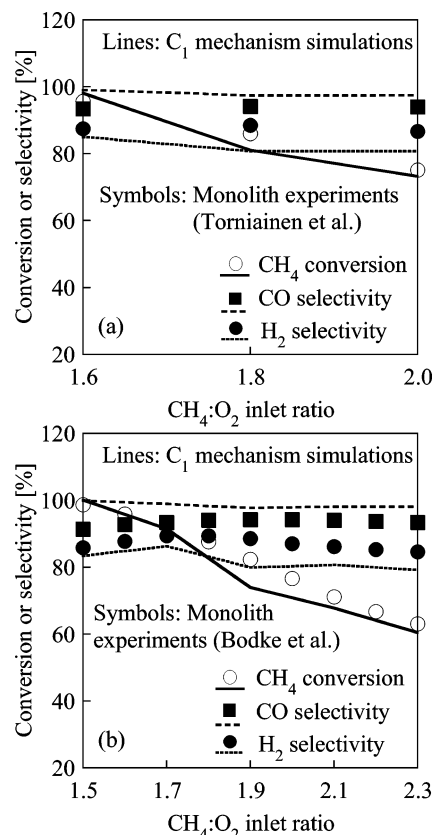


**Figure 18.** Panel a shows the predictions of the C<sub>1</sub> mechanism against the monolith reactor experiments of ref 47. The operating conditions include a pressure of 1.4 atm, a reactor volume of ~2.3 cm<sup>3</sup>, a catalyst area of ~255.1 cm<sup>2</sup>, and an inlet flow rate of 4 L/min at STP (note that the inlet velocity changes with temperature). The feed includes 5% air. Predictions against the monolith reactor experiments of refs 48 and 49 are shown in panel b. The operating conditions include a pressure of 1.2 atm, a reactor volume of ~2 cm<sup>3</sup>, a catalyst area of ~229 cm<sup>2</sup>, and an inlet flow rate of 5 L/min at STP (note that the inlet velocity changes with temperature). The feed includes 30% N<sub>2</sub>.

with the experimental data, as shown in Figure 18 (panel b), when the simulation temperatures are increased by 150 °C. The mole fraction profiles (not shown) for both experiments, as a

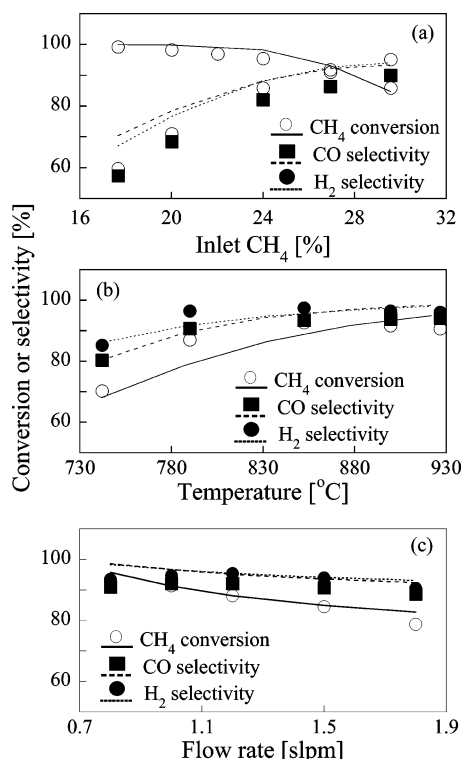


**Figure 19.** Validation of the C<sub>1</sub> mechanism against the fluidized bed reactor experimental data of ref 41 regarding the effect of inlet composition (panel a), bed temperature (panel b), and inlet flow rate (panel c). The operating conditions are the same as in Figure 12.

function of reactor length, provide similar information as the honeycomb and microlith experiments described in the main paper (see Figures 6 and 8). At the front of the reactor, a combination of partial and complete oxidation products (CO and H<sub>2</sub>O) are observed, followed by steam reforming that results in H<sub>2</sub> production.

**Predictions against Fluidized Bed Reactor Data.** Fluidized bed experiments were carried out by Bharadwaj and Schmidt to investigate the effect of inlet composition, bed temperature, and inlet flow rate on CH<sub>4</sub> conversion and syngas selectivity.<sup>41</sup> Since the fluidized bed is more mixed, better temperature uniformity, probably within 50–100 °C, could be achieved. Here, we employ a simple CSTR model to evaluate the performance of the C<sub>1</sub> mechanism. Figure 19 shows the predictions using the C<sub>1</sub> mechanism against these experiments. In panels a (effect of inlet composition) and b (effect of bed temperature), we have decreased the reported bed temperature by 30 and 65 °C, respectively. In panel c (effect of inlet flow rate), where a constant external heat input was used and bed temperatures were not reported, the temperature at one experimental point is adjusted to capture the CH<sub>4</sub> conversion. Using a nonisothermal CSTR, the amount of external heat input is derived to predict that temperature and finally, all remaining temperatures at other experimental conditions are predicted using the same external heat input. The effects of inlet composition, bed temperature, and inlet flow rate are well captured by the C<sub>1</sub> mechanism, as shown in Figure 19.

RPA for the conditions in Figure 19 (panel a, effect of inlet composition) shows that the thermal decomposition of CH<sub>4</sub> dominates over the oxidative dehydrogenation (using O\* or OH\*). This is a different inference from the Rh honeycomb or monoliths and is mainly due to the well-mixed nature of a fluidized bed. Distinct oxidation and reforming regions are not observed due to the absence of any spatial gradients in the

model. A pairwise brute force SA is carried out to identify the rate-determining step (RDS) for CH<sub>4</sub> conversion, CO selectivity, and H<sub>2</sub> selectivity. R<sub>80</sub> (C\* + OH\* → CO\* + H\*) is found to be the RDS for all model responses in these fluidized bed experiments. Using RPA, it is confirmed that R<sub>80</sub> is not in partial equilibrium (PE) and is the most important path in CO\* production. It is the most dominant H\* production path as well (other dominant H\* production paths of thermal CH<sub>x</sub> decomposition are in PE). Similar RPA is observed for panels b (effect of bed temperature) and c (effect of inlet flow rate).

## References and Notes

- (1) Ogden, J. M. *Annu. Rev. Energy Environ.* **1999**, *24*, 227.
- (2) Ballard. [http://www.ballard.com/be\\_informed/about\\_ballard](http://www.ballard.com/be_informed/about_ballard).
- (3) Hickman, D. A.; Schmidt, L. D. *Science* **1993**, *259*, 343.
- (4) Aghalayam, P.; Park, Y. K.; Vlachos, D. G. *Detailed surface reaction mechanisms for methane oxidation on platinum*; Joint Combustion Meeting of the U.S. Sections of the Combustion Institute, March 14–17, 1999, Washington, DC.
- (5) Aghalayam, P.; Park, Y. K.; Vlachos, D. G. *Partial oxidation of light alkanes in short contact time microreactors*, *Catalysis*; The Royal Society of Chemistry: Cambridge, U.K., 2000; Vol. 15.
- (6) Aghalayam, P.; Park, Y. K.; Vlachos, D. G. *AIChE J.* **2000**, *46*, 2017.
- (7) Park, Y. K.; Aghalayam, P.; Vlachos, D. G. *J. Phys. Chem. A* **1999**, *103*, 8101.
- (8) Mhadeshwar, A. B.; Wang, H.; Vlachos, D. G. *J. Phys. Chem. B* **2003**, *107*, 12721.
- (9) Deshmukh, S. R.; Mhadeshwar, A. B.; Lebedeva, M.; Vlachos, D. G. *Int. J. Multiscale Comput. Eng.* **2004**, *2*, 221.
- (10) Mhadeshwar, A. B.; Vlachos, D. G. *J. Phys. Chem. B* **2004**, *108*, 15246.
- (11) Mhadeshwar, A. B.; Vlachos, D. G. *J. Catal.* **2005**, *234*, 48.
- (12) Aghalayam, P.; Park, Y. K.; Fernandes, N. E.; Papavassiliou, V.; Mhadeshwar, A. B.; Vlachos, D. G. *J. Catal.* **2003**, *213*, 23.
- (13) Desai, S. K.; Neurock, M.; Kourtakakis, K. *J. Phys. Chem. B* **2002**, *106*, 2559.
- (14) Gokhale, A. A.; Kandoi, S.; Greeley, J.; Mavrikakis, M.; Dumesic, J. A. *Chem. Eng. Sci.* **2004**, *59*, 4679.
- (15) Dumesic, J. A.; Rudd, D. F.; Aparicio, L. M.; Rekoske, J. E.; Trevino, A. A. *The Microkinetics of Heterogeneous Catalysis*; American Chemical Society: Washington, D.C., 1993.
- (16) Brass, S. G.; Ehrlich, G. *J. Chem. Phys.* **1987**, *87*, 4285.
- (17) Mavrikakis, M. Personal communication, 2004.
- (18) Liu, Z.-P.; Hu, P. *J. Am. Chem. Soc.* **2003**, *125*, 1958.
- (19) Shustorovich, E.; Sellers, H. *Surf. Sci. Rep.* **1998**, *31*, 1.
- (20) Shustorovich, E. *Adv. Catal.* **1990**, *37*, 101.
- (21) Parmeter, J. E.; Jiang, X.; Goodman, D. W. *Surf. Sci.* **1990**, *240*, 85.
- (22) Kua, J.; Goddard III, W. A. *J. Am. Chem. Soc.* **1999**, *121*, 10928.
- (23) Coltrin, M. E.; Kee, R. J.; Rupley, F. M. Surface Chemkin (version 4.0): A FORTRAN package for analyzing heterogeneous chemical kinetics at a solid-surface–gas-phase interface; Sandia National Laboratories Report No. SAND90-8003B; Livermore, CA, 1991.
- (24) Raimondeau, S.; Vlachos, D. G. *Chem. Eng. J.* **2002**, *90*, 3.
- (25) Mhadeshwar, A. B.; Vlachos, D. G. *Combust. Flame* **2005**, *142*, 289.
- (26) Fichtner, M.; Mayer, J.; Wolf, D.; Schubert, K. *Ind. Eng. Chem. Res.* **2001**, *40*, 3475.
- (27) GRI Gas-Research-Institute mechanism for natural gas (3.0); taken from [http://www.me.berkeley.edu/gri\\_mech/](http://www.me.berkeley.edu/gri_mech/), 1999.
- (28) Hammer, B.; Nielsen, O. H.; Mortensen, J. J.; Bengtsson, L.; Hansen, L. B.; Madsen, A. C. E.; Morikawa, Y.; Bligaard, T.; Christensen, A. DCAPO version 2.7 (CAMP, Technical University, Denmark).
- (29) Vanderbilt, D. *Phys. Rev. B* **1990**, *41*, 7892.
- (30) Marinov, N. M.; Pitz, W. J.; Westbrook, C. K.; Vincitore, A. M.; Castaldi, M. J.; Senkan, S. M. *Combust. Flame* **1998**, *114*, 192.
- (31) Lyubovskiy, M.; Roychoudhury, S.; R., L. *Catal. Lett.* **2005**, *99*, 113.
- (32) Deutschmann, O.; Schwiedernoch, R.; Maier, L. I.; Chatterjee, D. *Nat. Gas Convers. VI, Stud. Surf. Sci. Catal.* **2001**, *136*, 251.
- (33) Deutschmann, O.; Schmidt, L. D. *Proc. Combust. Inst.* **1998**, *27*, 2283.
- (34) Tsang, S. C.; Claridge, J. B.; Green, M. L. H. *Catal. Today* **1995**, *23*, 3.
- (35) Schwiedernoch, R.; Tischer, S.; Correa, C.; Deutschmann, O. *Chem. Eng. Sci.* **2003**, *58*, 633.
- (36) Slaa, J. C.; Berger, R. J.; Marin, G. B. *Catal. Lett.* **1997**, *43*, 63.
- (37) Hickman, D. A.; Schmidt, L. D. *AIChE J.* **1993**, *39*, 1164.



- (38) Mallens, E. P. J.; Hoebink, J. H. B. J.; Marin, G. B. *J. Catal.* **1997**, *167*, 43.
- (39) Hofstad, K. H.; Hoebink, J. H. B. J.; Holmen, A.; Marin, G. B. *Catal. Today* **1998**, *40*, 157.
- (40) Vesper, G.; Frauhammer, J. *Chem. Eng. Sci.* **2000**, *55*, 2271.
- (41) Bharadwaj, S. S.; Schmidt, L. D. *J. Catal.* **1994**, *146*, 11.
- (42) Bergald, J.; Kasemo, B.; Chakarov, D. V. *Surf. Sci.* **2001**, *495*, L815.
- (43) Basini, L.; Sanfilippo, D. *J. Catal.* **1995**, *157*, 162.
- (44) Zum Mallen, M. P.; Schmidt, L. D. *J. Catal.* **1996**, *161*, 230.
- (45) Papapolymerou, G. A.; Schmidt, L. D. *Langmuir* **1987**, *3*, 1098.
- (46) Wei, D. H.; Skelton, D. C.; Kevan, S. D. *Surf. Sci.* **1997**, *381*, 49.
- (47) Torniaainen, P. M.; Chu, X.; Schmidt, L. D. *J. Catal.* **1994**, *146*, 1.
- (48) Bodke, A. S.; Bharadwaj, S. S.; Schmidt, L. D. *J. Catal.* **1998**, *179*, 138.
- (49) Goralski Jr., C. T.; O'Connor, R. P.; Schmidt, L. D. *Chem. Eng. Sci.* **2000**, *55*, 1357.
- (50) Fisher, G. B.; Schmieg, S. J. *J. Vac. Sci. Technol., A* **1983**, *1*, 1064.
- (51) Root, T. W.; Schmidt, L. D. *Surf. Sci.* **1983**, *134*, 30.
- (52) Savchenko, V. I.; Boreskov, G. K.; Kalinkin, A. V.; Salanov, A. N. *Kinet. Catal.* **1983**, *24*, 983.
- (53) Wilke, S.; Natoli, V.; Cohen, M. H. *J. Chem. Phys.* **2000**, *112*, 9986.
- (54) Hansen, E. W.; Neurock, M. *Surf. Sci.* **1999**, *441*, 410.
- (55) Loffreda, D.; Simon, D.; Sautet, P. *J. Chem. Phys.* **1998**, *108*, 6447.
- (56) Smedh, M.; Beutler, A.; Borg, M.; Nyholm, R.; Anderson, J. N. *Surf. Sci.* **2001**, *491*, 115.
- (57) He, R.; Kusaka, H.; Mavrikakis, M.; Dumesic, J. A. *J. Catal.* **2003**, *217*, 209.
- (58) Thiel, P. A.; Williams, E. D.; Yates, J. T.; Weinberg, W. H. *Surf. Sci.* **1979**, *84*, 54.
- (59) Zhang, C. J.; Hu, P.; Lee, M.-H. *Surf. Sci.* **1999**, *432*, 305.
- (60) Mavrikakis, M.; Baumer, M.; Freund, H.-J.; Norskov, J. K. *Catal. Lett.* **2002**, *81*, 153.
- (61) Hendrickx, H. A. C. M.; Jongenelis, A. P. J. M.; Nieuwenhuys, B. E. *Surf. Sci.* **1985**, *154*, 503.
- (62) Brown, L. S.; Sibener, S. J. *J. Chem. Phys.* **1989**, *90*, 2807.
- (63) Hei, M. J.; Chen, H. B.; Yi, J.; Lin, Y. J.; Lin, Y. Z.; Wei, G.; Liao, D. W. *Surf. Sci.* **1998**, *417*, 82.
- (64) Payne, S. H.; Kreuzer, H. J.; Frie, W.; Hammer, L.; Heinz, K. *Surf. Sci.* **1999**, *421*, 279.
- (65) Wilke, S.; Hennig, D.; Lober, R. *Phys. Rev. B* **1994**, *50*, 2548.
- (66) Mavrikakis, M.; Rempel, J.; Greeley, J.; Hansen, L. B.; Norskov, J. K. *J. Chem. Phys.* **2002**, *117*, 6737.
- (67) Eichler, A.; Hafner, J.; Kresse, G. *J. Phys.: Condens. Matter* **1996**, *8*, 7659.
- (68) Zinck, J. J.; Weinberg, W. H. *J. Vac. Sci. Technol.* **1980**, *17*, 188.
- (69) Feibelman, P. J. *Phys. Rev. Lett.* **2003**, *90*, 186103.
- (70) Sant, R.; Wolf, E. E. *Chem. Eng. Sci.* **1990**, *45*, 3137.
- (71) Gopinath, C. S.; Zaera, F. J. *Catal.* **2001**, *200*, 270.
- (72) Coulston, G. W.; Haller, G. L. *J. Chem. Phys.* **1991**, *95*, 6932.
- (73) Hopstaken, M. J. P.; Niemantsverdriet, J. W. *J. Chem. Phys.* **2000**, *113*, 5457.
- (74) Klotzer, B.; Unterberger, W.; Hayek, K. *Surf. Sci.* **2003**, *532*–535, 142.
- (75) Zum Mallen, M. P.; Williams, W. R.; Schmidt, L. D. *J. Phys. Chem.* **1993**, *97*, 625.
- (76) Gregoratti, L.; Baraldi, A.; Dhanak, V. R.; Comelli, G.; Kiskinova, M.; Rosei, R. *Surf. Sci.* **1995**, *340*, 205.
- (77) Yates, J. T.; Thiel, P. A.; Weinberg, W. H. *Surf. Sci.* **1979**, *84*, 427.
- (78) Schennach, R.; Krenn, G.; Klotzer, B.; Rendulic, K. D. *Surf. Sci.* **2003**, *540*, 237.
- (79) Pauer, G.; Eichler, A.; Sock, M.; Ramsey, M. G.; Netzer, F.; Winkler, A. *J. Chem. Phys.* **2003**, *119*, 5253.
- (80) Gibson, K. D.; Viste, M.; Sibener, S. J. *J. Chem. Phys.* **2000**, *112*, 9582.
- (81) Panagiotopoulou, P.; Kondarides, D. I. *J. Catal.* **2004**, *225*, 327.
- (82) Han, Y.-F.; Kahlich, M. J.; Kinne, M.; Behm, R. J. *Appl. Catal. B: Environ.* **2004**, *50*, 209.
- (83) Zhang, Z.; Kladi, A.; Verykios, X. E. *J. Catal.* **1994**, *148*, 737.
- (84) Morley, C. "GASEQ: Chemical equilibria in perfect gases, version 0.75b".
- (85) <http://dion.che.Udel.edu>